SPACE TELESCOPE SCIENCE INSTITUTE

Hubble Space Telescope

Optical Telescope Assembly

Handbook

Version 1.0

May 1990

Revision History
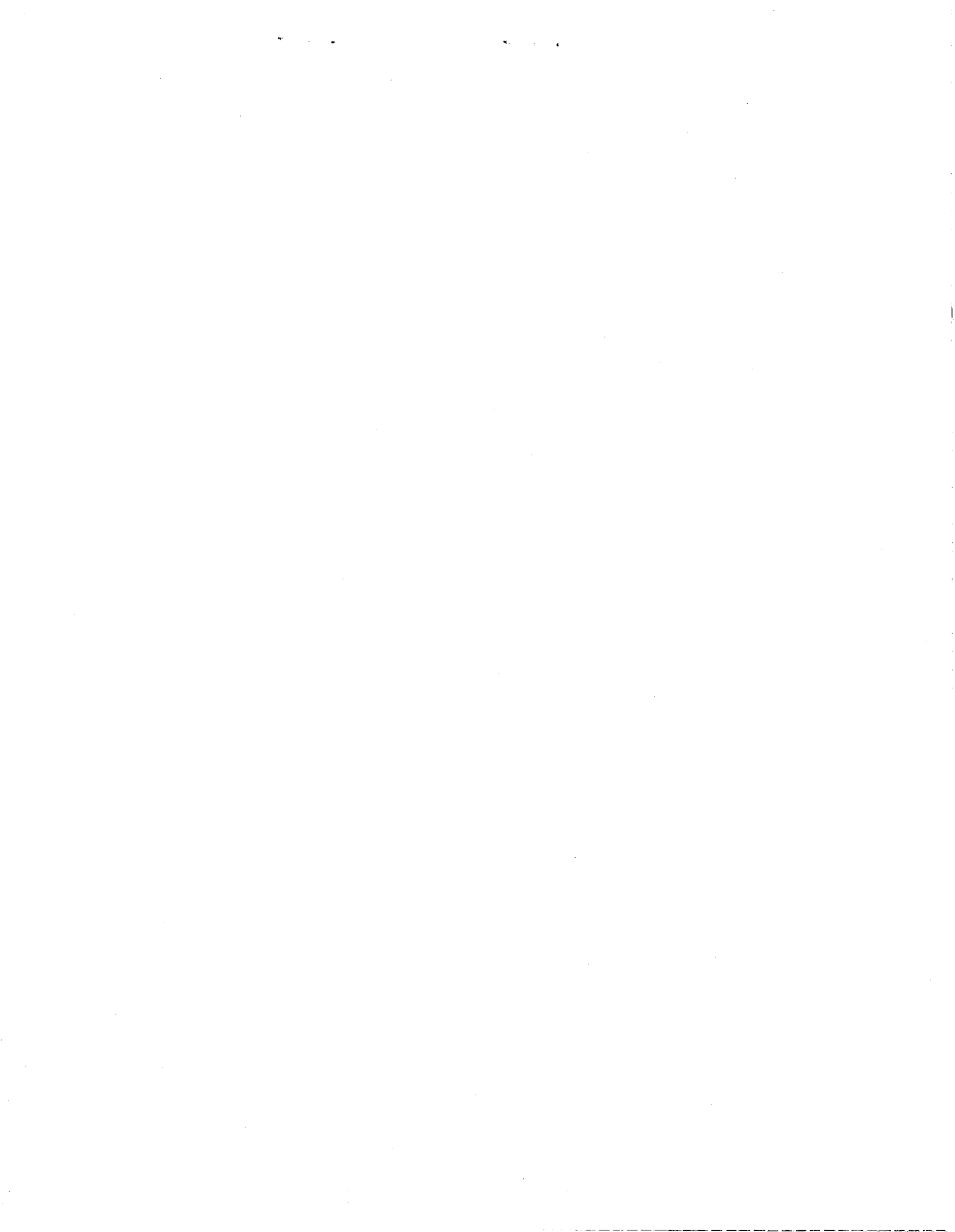
DISPLAY 92N17483/2
92N17483*#   ISSUE 8   PAGE 1386   CATEGORY 89   RPT#: NASA-CR-189751 NAS
1.26:189751   CNT#: NAS5-26555   90/05/00   67 PAGES   UNCLASSIFIED
DOCUMENT
Revised
UTTL: Hubble Space Telescope: Optical telescope assembly handbook. Version 1.0
AUTH: A/BURROWS, CHRIS
CORP: Space Telescope Science Inst., Baltimore, MD.
SAP: Avail: NTIS HC/MF A04
CIO: UNITED STATES
MAJS: /*FOCAL PLANE DEVICES/*HANDBOOKS/*HUBBLE SPACE TELESCOPE/*POINT SOURCES
MINS: / IMAGING TECHNIQUES/ SIMULATION/ SYSTEMS ANALYSIS
ABA: Author
ABS: The Hubble Space Telescope is described along with how its design affects
     the images produced at the Science Instruments. An overview is presented
     of the hardware. Details are presented of the focal plane, throughput of
     the telescope, and the point spread function (image of an unresolved point
     source). Some detailed simulations are available of this, which might be
     useful to observers in planning their observations and in reducing their
     data.

ENTER:

CONTENTS

1.0 PURPOSE

This document describes the Hubble Space Telescope and how its design affects the images produced at the Science Instruments. This introductory chapter contains an overview of the hardware. Subsequent chapters detail the geometry of the focal plane, throughput of the telescope, and the point-spread function (image of an unresolved point source). Some detailed simulations are available of this, which might be useful to observers in planning their observations and in reducing their data.

The present version of this document has been produced to meet the needs of General Observers preparing their Phase II inputs on programs recommended by the Time Allocation Committee. It is still in a preliminary form, as timeliness was considered important. It consists of essentially unedited extracts from a Lockheed publication to provide a system-level overview. This section will help General Observers to understand the complexity of the system they are to operate, and some of its constraints and limitations. The rest of the document is the responsibility of the author. It consists mainly of edited internal reports, together with some new material.

The author would like to thank scientific colleagues who have contributed to this document. In particular Hashima Hasan for excellent help in developing the imaging simulation program described here. Robert Brown and Peter Stockman for many useful discussions and contrubutions particularly on the mirror microroughness and dust modelling. Keith Horne and Jan Koornneef for provision of Instrument sensitivities and XCAL interface to them. Finally thanks to Bruce Gillespie, Howard Bond and the staff of the Business Systems Support Group for help in the production and proofreading.

1.1 ACRONYMS AND ABBREVIATIONS

A	Angstrom (10^{-10} m)
AB	Aft Bulkhead
ACE	Actuator Control Electronics
ACS	Actuator Control Subsystem
AS	Aft Shroud
BAe	British Aerospace
BASD	Ball Aerospace Systems Divsion
C&DH	Communication and Data Handling
CBA	Central Baffle Assembly
CCD	Charge-Coupled Device
CEU	Camera Electronics Unit
CIT	California Institute of Technology
CPU	Central Processing Unit
CSS	Course Sun Sensor
CU/SDF	Control Unit/Science Data Formatter
DCF	Data Capture Facility
DH	Data Handling
DMA	Direct Memory Access
DMU	Data Management Unit

DSASS   Digital Sun Angle Sensing System

ECA   Electronics Control Assembly
ED   Engineering Data
EMI   Electromagnetic Interference
EPS   Electrical Power Subsystem
EPTCE   Electrical Power Thermal Control Electronics
ES   Equipment Section, Equipment Shelf
ESA   European Space Agency
ESTR   Engineering and Science Tape Recorder
EVA   Extravehicular Activity

FCA   Figure Control Actuator
FFT   Front Fournier Transform
FGE   Fine Guidance Electronics
FGS   Fine Guidance Sensor
FHST   Fixed Head Star Tracker
FOC   Faint Object Camera
FOS   Faint Object Spectrograph
FOV   Field of View
FPA   Focal Plane Assembly
FPS   Focal Plane Structure

GE   General Electric
GEA   Gimbal Electronics Assembly
GGM   Gravity Gradient Mode
GSE   Ground Support Equipment
GSFC   Goddard Space Flight Center (Maryland)
GSTDN   Ground Spaceflight Tracking and Data Network

HGA   High Gain Antenna
GHRS   Goddard High Resolution Spectrograph
HSP   High Speed Photometer
HST   Hubble Space Telescope
Hz   Hertz (Cycles per Second)

I&C   Instrumentation and Communications (subsystem)
IBM   International Business Machines Corporation
ICU   Instrumentation Control Unit
IDCA   Image Disector Camera Assembly
IDT   Instrument Development Team
IOU   Input Output Unit
IR   Infrared

JHU   The Johns Hopkins University
JPL   Jet Propulsion Laboratory
JSC   Johnson Space Center

KBPS   Kilobits per Second

Kbytes Kilobytes
KSC Kennedy Space Center

LGA Low Gain Antenna
LLD Low Level Discrete
LMSC Lockheed Missiles & Space Company, Inc.
LOS Line of Sight
LS Light Shield

M&R Maintenance and Refurbishment
MCE Monitor and Control Electronics
MCU Mechanisms Control Unit
MgF2 Magnesium Fluoride
MIT Massachusetts Institute of Technology
MLI Multilayer Insulation
MMC Martin Marietta Corporation
MOGS Mission Operations Ground System
MSFC Marshall Space Flight Center
MSS Magnetic Sensing System
MT Magnetic Torquer
MTA Metering Truss Assembly
MTB Magnetic Torque Bar
MTE Magnetic Torquer Electronics
MTF Modulation Transfer Function
MTS Metering Truss Structure
MU Memory Unit
Mv Apparent Visual Magnitude

N/A Not Applicable
NASA National Aeronautics and Space Administration
NASCOM NASA Communications Network
NCC Network Control Center
NCCDS Network Control Data System
nm Nanometers (10^{-9} meters)
NOCC Network Operations Control Center
NSSC-I NASA Standard Spacecraft Computer, Model-I

OB Optical Bench
OBC On-Board Computer
OCE Optical Control Electronics
OCS Optical Control Subsystem
OSCF Operation Support Computing Facility
OLD Off-Load Device
ORU Orbital Replaceable Unit
OSS Office of Space Science
OSFC Operations Support Computing Facility
OSTDS Office of Space Tracking and Data Systems

OTA   Optical Telescope Assembly
OTF   Optical Transfer Function

P-E   Perkin-Elmer Corporation
PASS   POCC Application Software Support
PC   Planetary Camera
PCEA   Pointing Control Electronics Assembly
PCS   Pointing Control Subsystem
PCU   Power Control Unit; Power Convertor Unit (module of DF-224)
PDM   Primary Drive Motor, Primary Deployment Mechanism
PDU   Power Distribution Unit
PI   Principal Investigator
PM   Primary Mirror
PMT   Photomultiplier Tube
POCC   Payload Operations Control Center
POS   Position
PRLA   Payload Retention Latch Assemblies
PSEA   Pointing/Safing Electronics Assembly
PSF   Point Spread Function

RCS   Reaction Control System
RDA   Rotary Drive Actuator
RFI   Radio Frequency Interference
RGA   Rate Gyro Assembly
RIG   Rate Integration Gyros
RIU   Remote Interface Unit
RMES   Retrieval Mode Electronics Assembly
RMGA   Retrieval Mode Gyro Assembly
RMS   Remote Manipulator System
ROM   Read-Only Memory
RPA   Reactive Plate Assembly
RSU   Rate Sensing Unit
RTC   Real Time Command
RWA   Reaction Wheel Assembly

S/N   Signal-to-Noise Ratio
SAA   South Atlantic Anomaly
SBA   Secondary Baffle Assembly
SDF   Science Data Formatter
SI   Scientific Instrument
SI C&DH   SI Control and Data Handling (subsystem)
SIMA   Secondary Mirror Incremental Motor Actuator
SM   Secondary Mirror
SMB   Secondary Mirror Baffle
SSA   Star Selector Assembly
SSM   Support Systems Module

SSS	Star Selector Servos
STDN	Space (flight) Tracking and Data Network
STOCC	Space Telescope Operations Control Center
STS	Space Transportation System
ST ScI	Space Telescope Science Institute

TBD	To Be Determined
TCS	Thermal Control Subsystem
TDRS	Tracking and Data Relay Satellite
TDRSS	Tracking and Data Relay Satellite System
TIM	Telescope Image Modelling Software
TR	Tape Recorder
TRW	Thompson Ramo Woolridge, Inc.
TV	Thermal Vacuum

UC	University of California
UCSD	University of California, San Diego
ULE	Ultra Low Expansion
UT	University of Texas
UV	Ultraviolet

V1,V2,V3	ST Coordinate System

WFC	Wide Field Camera
WF/PC	Wide Field Planetary Camera

1.2   SPACE TELESCOPE SCIENTIFIC OVERVIEW

The following sections are edited from the Space Telescope Systems Descriptions Handbook, ST-SE-02. It represents a compilation of current data and descriptive information extracted from several sources.

The objective of the Space Telescope Project is to orbit a high quality optical 2.4-m telescope system by the Space Shuttle for use by the astronomical community. The scientific objectives of the Space Telescope are to determine the constitution, physical characteristics, and dynamics of celestial bodies, the nature of processes which occur in the extreme physical conditions existing in stellar objects; the history and evolution of the universe; and whether the laws of nature are universal.

Like ground-based telescopes, the Hubble Space Telescope was designed as a general-purpose instrument, capable of utilizing a wide variety of scientific instruments at its focal plane. By using the Space Shuttle to provide scientific instrument upgrading and subsystems maintenance, the useful and effective operational lifetime of the Space Telescope will be extended to a decade or more.

Ground-based telescopes can recognize individual galaxies several billion light years away. However, all earthbound devices have limited resolution because of the blurring effect which the earth's atmosphere causes due to its turbulence and light scattering. The wavelength region observable from the earth's surface is limited by the atmosphere to the visible part of the spectrum. Unlike ground-based telescopes, the 2.4-m Space Telescope will possess and can effectively utilize an optical quality of such precision that its resolving power is

limited primarily by the diffraction of the optics. The Space Telescope will be taken into earth orbit by the Space Shuttle and, from there, unhindered by atmospheric distortion and absorption, it can see objects with a resolution approximately seven to ten times better than that obtainable even with the largest telescopes on earth and over a wavelength region which reaches far into the ultraviolet (UV) and eventually infrared (IR) portions of the spectrum. Objects at seven billion light years, for example, can be seen with the Space Telescope with as much detail as objects at one billion light years can be seen with the best earthbound telescopes. And more important, objects which are lost in the sky background to ground-based telescopes will be seen for the first time by HST.

The overall scientific objectives are to gain a significant increase in our understanding of the universe through observations of celestial objects and events. The HST has been designed to achieve the following specific scientific objectives:

- Precise determination of distances to galaxies out to expansion velocities of 1×10^4 km/sec and calibration of distance criteria applicable at cosmologically significant distances.
- Determination of the rate of the deceleration of the Hubble expansion of the universe, its uniformity in different directions, and possibly its constancy with time.
- Testing of the reality of the universal expansion by determination of the surface brightness versus redshift relation for distant galaxies.
- Establishment of the history of star formation and nuclear processing of matter as a function of position in nearby galaxies and determination of the variations from galaxy to galaxy.
- Determination of the nature of stellar populations in the early stages of galactic evolution, based on "lookback" observation of distant galaxies.
- Estimation of the He/H ratio in quasars by observation of the red-shifted He I and He II resonance lines.
- Search for multiple-red-shift absorption line groups in the ultraviolet spectra of low-red-shift quasars.
- Intercomparison of total spectra of high-red-shift quasars, low-red-shift quasars, and active galactic nuclei.
- Resolution of densely-packed nuclei of globular star clusters.
- Identification and flux measurements in ultraviolet and optical wavelengths of faint X-ray sources and radio pulsars.
- Resolution of the complex internal structure of Herbig-Haro objects to investigate their links to star formation.
- High spatial resolution observations of proto-stars.
- Possible direct imaging and astrometric search for planetary companions of nearby stars.
- Determination of the bolometric luminosities of faint, hot stars for studies of stellar evolution.
- Determination of composition, temperature, density, and ionization structure of the gas in the galactic halo, in high-velocity clouds, and in the intergalactic medium.
- Precise mapping of the 100μm flux sources in compact H II regions.
- Determination of the composition of clouds in the atmospheres of Jupiter, Saturn, Uranus, and Neptune.
- Resolution of surfaces of minor planets and asteroids.

- Synoptic mapping of atmospheric features on Jupiter, Saturn, and Uranus for study of atmospheric dynamics.
- Intensity measurements of atomic and molecular ultraviolet emission lines important to understanding the chemistry of comets.

The primary objective of HST design and development is to provide a high resolution, optical telescope system that will meet these scientific objectives and perform them within the operational life of the HST.

The scientific and technological requirements will be fulfilled within the anticipated mission operational life of 15 years. In principle there is no reason the mission operation could not be operated for many decades. Because the Science Instruments (SIs) and some of the electronics are of modular design they can be replaced with improved or different models. Periodic orbital maintenance and altitude reboost via the Shuttle Orbiter is planned. If major refurbishing is necessary it may be possible to retrieve the ST, return it to earth and relaunch.

1.3 SPACECRAFT OVERVIEW

The NASA Hubble Space Telescope (HST) is an astronomical observatory to be placed in an approximately circular orbit at 593 km (320 NM) altitude, at an inclination angle of 28.5° and an orbital period of approximately 95 min. Operating well above the earth's turbulent atmosphere, HST will: observe the ultraviolet, visible, and infrared wavelength regions of the faintest objects; achieve an increase in spatial resolution that is seven or more times better than the capability of ground-based observatories for a wide range of objects; detect objects approximately 50 times fainter than are presently observable and view them with ten times better clarity than ground-based observatories. This capability will expand the universe visible to man by 350 times and enable him to see close to the edge of the observable universe, an estimated 14 billion light years away.

1.3.1 General Configuration

The HST launch weight will be approximately 11,600 kg (25,500 lb); it will be 13.1 m (43.5 ft) long and have a diameter of 4.27 m (14 ft) at the aft end and have a diameter of 3.05 m (10 ft) at the forward end. The spacecraft illustrated in Figure 1.1 is built to work much like a ground observatory. In principle, it is no different than the reflecting telescopes invented by Guillaume Cassegrain and James Gregory in the 17th Century. This figure defines the location of the HST's major external surface elements and the cutaway section views some of the major support sections. Figure 1.2 is an exploded view of the HST modules to show their relative positions.

1.3.1.1 External Structure

- The support System Module (SSM) is divided into four main sections; the Light Shield (LS), the Forward Shell (FS), the Equipment Section (ES), and the Aft Shroud (AS). These four pieces fit together like stacked canisters, to enclose the Optical Telescope Assembly (OTA), Scientific Instruments (SIs), and electrical/mechanic modules to provide power, communications, pointing and control, and other support systems required for successful operation.

- The Aperture Door (AD) located at the ST forward end is attached to the SSM LS and is positioned to shade and protect the focal plane particularly from scattered earthshine.
- The Magnetic Torquers (MTs) are attached to the external surface of the SSM FS at four positions. The MTs are magnetized metal rods controlled by an onboard, triple-redundant computer to align the spacecraft with the earth's magnetic field. Working in conjunction with four attitude control reaction wheels located within SSM ES the attitude of the spacecraft may be controlled.
- High Gain Antennas (HGAs) are attached to the exterior surface of the SSM FS at two locations. While in the Shuttle bay the HGA is in a latched position located on the SSM LS. The reversible motor-driven hinge mechanism is used to deploy the HGA for on-orbit use or retracted for ST retrieval.
- The Solar Arrays (SAs) are attached to the exterior of the SSM FS at two locations. While in the Shuttle bay the SA is latched at a position located in the SSM LS. The deployed mechanism interfaces via an adapter with the Solar Array Drive Mechanism (SADM). The deployment and unfurling mechanisms are controlled by the Deployment Control Electronics (DCE).
- Handrails and portable foot restraints are fixed to the external surface to permit astronauts to perform Maintenance and Refurbishment (M&R) tasks.
- Access to many of these modules will be relatively easy as some compartments can be opened from the outside via a hatch or Access Door (AD). An astronaut opens the cover to get at the module needing replacement, disconnects the module from the plug-in compartment, and inserts a replacement. Among the components in the ES are the Reaction Wheel Assembly (RWA), Digital Interface Units (DIU), communication sytem, batteries, and charge controller. The AS fits over the section which contains the four axial SIs, one radial SI, and the three Fine Guidance Sensors (FGS). Access covers on this shroud enable astronauts to get at the other instruments such as the Fixed Head Star Tracker (FHST), Rate Gyro Assembly (RGA), and other sensors, for maintenance or removal.
- The Aft Bulkhead (AB) of the SSM AS contains four vents to equalize differential pressure during launch and recovery operations. An omnidirectional Low Gain Antenna (LGA) and two Coarse Sun Sensors (CSS) are also mounted to the AB.
- The OTA Equipment Section is a 150° toroidal structural assembly attached to the SSM FS and the forward face of the SSM ES. This section is slotted at the forward end for the HGA attachment to the FS.

1.3.1.2   Support Systems and Science Instruments

- The Focal Plane Structure (FPS) consists of a two-piece separable assembly consisting of the Focal Plane Deck Assembly (FPDA) and the Scientific Instrument Support Structure (SISS). The FPDA interfaces with the Main Ring (MR) and provides the forward support for the SSM Equipment Shelf (SSM-ES). The SISS supports the aft end of the SSM-ES.
- The three Fine Guidance Systems (FGSs) and the Wide Field/Planetary Camera (WF/PC), the only radial SI, are housed within the FPDA and are supported by latches to permit removal on orbit.
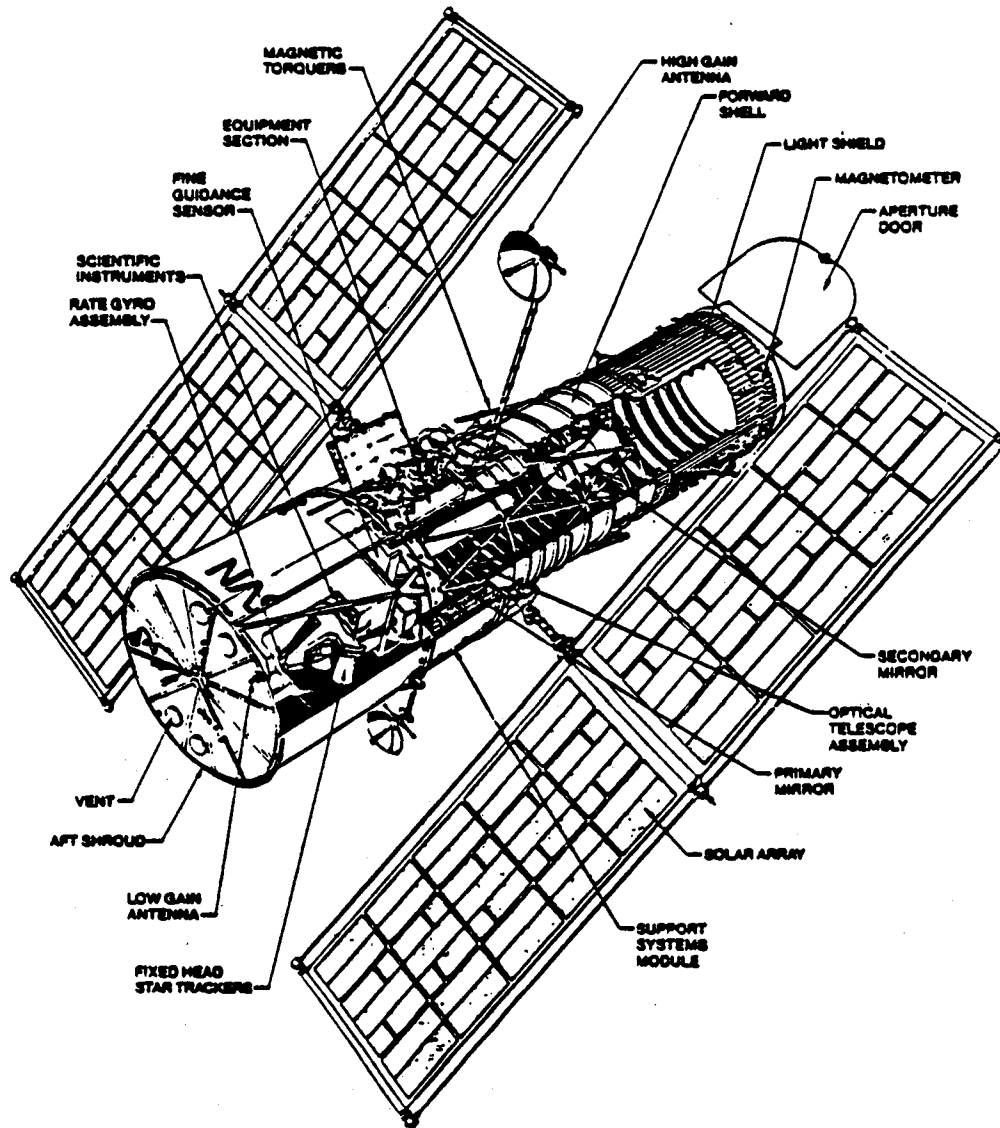
Figure 1.1 Hubble Space Telescope.

Figure 1.2 Space Telescope Exploded View.

MAGNETIC
TORQUER (4)

HIGH GAIN ANTENNA (2)

APERTURE
DOOR

SSM FORWARD SHELL

LIGHT
SHIELD

OTA SECONDARY
MIRROR ASSEMBLY

SECONDARY
MIRROR BAFFLE

OTA
METERING TRUSS

SSM EQUIPMENT
SECTION

OTA PRIMARY
MIRROR & MAIN RING

CENTRAL
BAFFLE

FINE GUIDANCE OPTICAL
CONTROL SENSOR (3)

OTA FOCAL PLANE
STRUCTURE

AXIAL SI
MODULE (4)

SOLAR ARRAY (2)

MAIN BAFFLE

RADIAL SI
MODULE (1)

SSM AFT
SHROUD

FIXED HEAD STAR TRACKER &
RATE GYRO ASSEMBLY

OTA EQUIPMENT
SECTION

- The Faint Object Spectrograph (FOS), Goddard High Resolution Spectrograph (GHRS), High Speed Photometer (HSP), and the Faint Object Camera (FOC) are the four axial SIs mounted in the SISS and supported by latches to permit removal on orbit.
- The Fixed Head Star Tracker (FHST) and three rate gyro assemblies called the Rate Sensor Units (RSUs) are mounted to the SSM-ES.
- The Main Ring Assembly (MRA) is the primary load carrying structure to which all OTA subassemblies such as the Primary Mirror Assembly (PMA), Secondary Mirror Assembly (SMA), Focal Plane Structure Assembly (FPSA), Reaction Plate Assembly (RPA), Axial OTA/SSM Links, Tangential OTA/SSM Links and Main Baffle (MB) are attached.
- The Central Baffle Assembly (CBA) is located just in front of the Primary Mirror (PM), while a Secondary Baffle (SB) fits just behind the Seconday Mirror (SM).
- A large aluminum Main Baffle Assembly (MBA) extends from the PM to just beyond the SM and is supported by the MR. The SBA is located concentric with and just inside the Metering Truss Assembly (MTA).
- The OTA Metering Truss Assembly (MTA) separates and supports the MRA and the Secondary Mirror Subassembly (SMSA).

1.3.1.3 Coordinate Systems

Three coordinate systems are defined in Figure 1.3 for the Orbiter, HST, and the HST Solar Arrays (SA). While in the Orbiter payload bay the HST coordinates (V1, V2, V3) are related to the Orbiter coordinates (X, Y, Z). The SA coordinates (S1, S2, S3) are referenced to the SA attach points.

The V1 origin is 6.096/m (240-in.) behind a plane through the OTA/SSM interface on the ST centerline (optical axis). The ST centerline is identical to V1 axis and is positive toward the SSM aperture door. The V3 axis is perpendicular to the V1 axis and the SA drive axis and is positive along the nominal sun direction (solar arrays in the V1, V2 plane, the sun perpendicular to the active side of the SA). The V2 axis is parallel to the SA drive axis and directed to form a right-hand coordinate system. When the HST is in the Orbiter V1 = 0 is at Orbiter station X = 1250 in., V2 = 0 at Orbiter station Y = 0 and V3 = 0 at Orbiter station Z = 400 in.

In section 2.1 these physical coordinate systems are related to the focal plane and then projected both onto instrument apertures and the sky.

1.3.2 ST Major Elements

1.3.2.1 Support System Module (SSM)

The SSM (Figure 1.4) is the major component of the HST which houses the Optical Telescope Assembly (OTA), Scientific Instruments (SIs), and the Scientific Instruments Control and Data Handling (SI C&DH) Subsystem, and supports the OTA equipment section.

The physical relationship of the SSM, OTA, OTA equipment section, and SIs are shown in Figure 1.4. The SSM provides structural support, thermal control, electrical power, communications, data managment, pointing control in support of the OTA, OTA equipment section, SI, SI C&DH, and the ST system. The SSM structure is composed of the following major components: Aperature Door (AD), Light Shield (LS), SSM Forward Shell (FS), SSM

NOTES:

1. SA ZERO REF POSITION:
   S_3 PARALLEL TO -V1
2. SA REF ATTACH POINTS
   $(S_2 = 0)$:
   [V1 = 320, V2 = 80, V3 = 0]
                AND
   [V1 = 320, V2 = 80, V3 = 0]

3. REF POSITION OF ST CG WITHOUT SA
   [V1 = 253, V2 = 0, V3 = -2]

4. ST-TO-SHUTTLE STATION CONVER-
   SION FACTOR (WHEN THE ST IS IN
   THE ORBITER):
   $X_{orb} = 1250 - V_1$
   $Y_{orb} = +V_2$
   $Z_{orb} = 400 - V_3$

WHEN IN
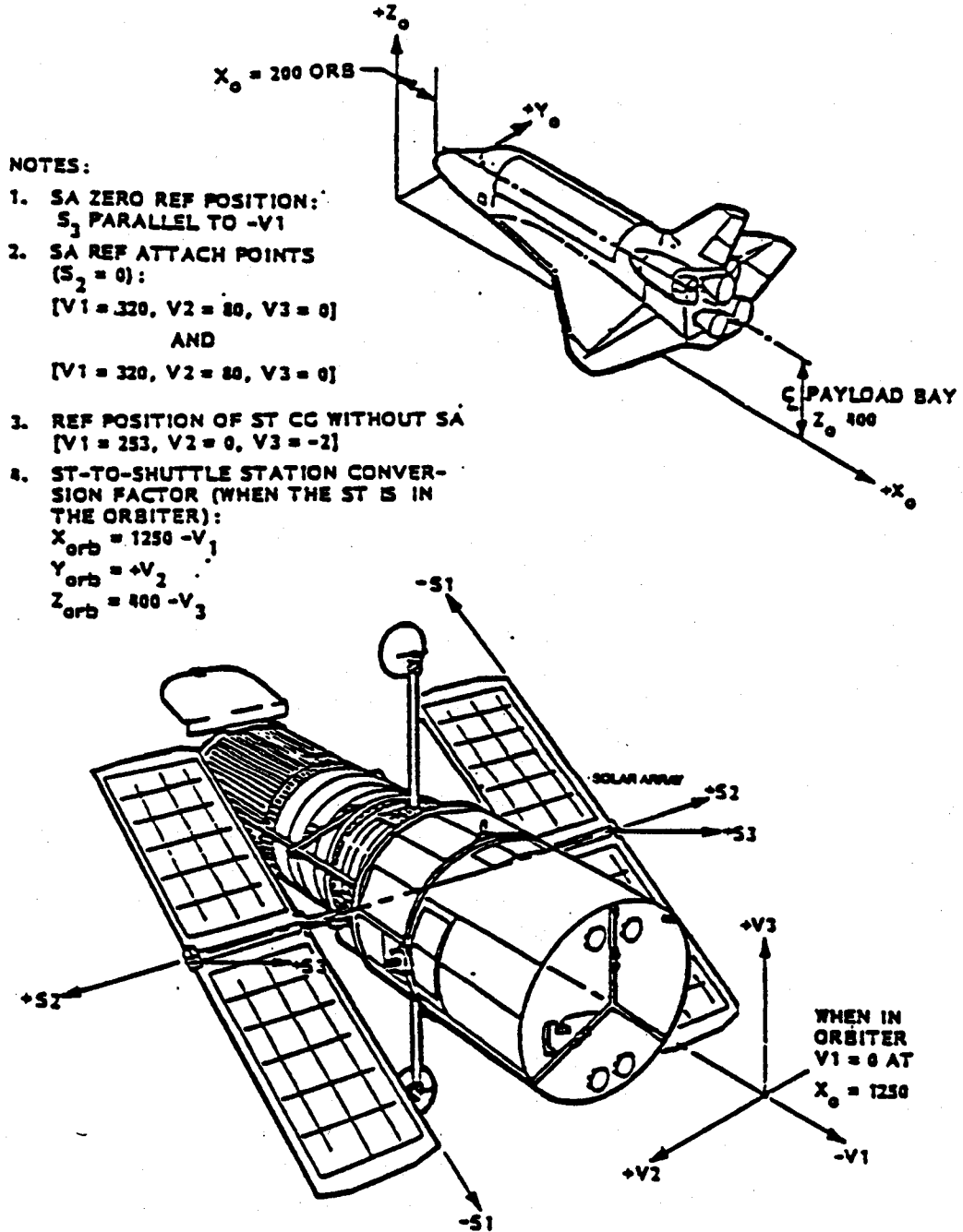ORBITER
V1 = 0 AT
$X_0 = 1250$

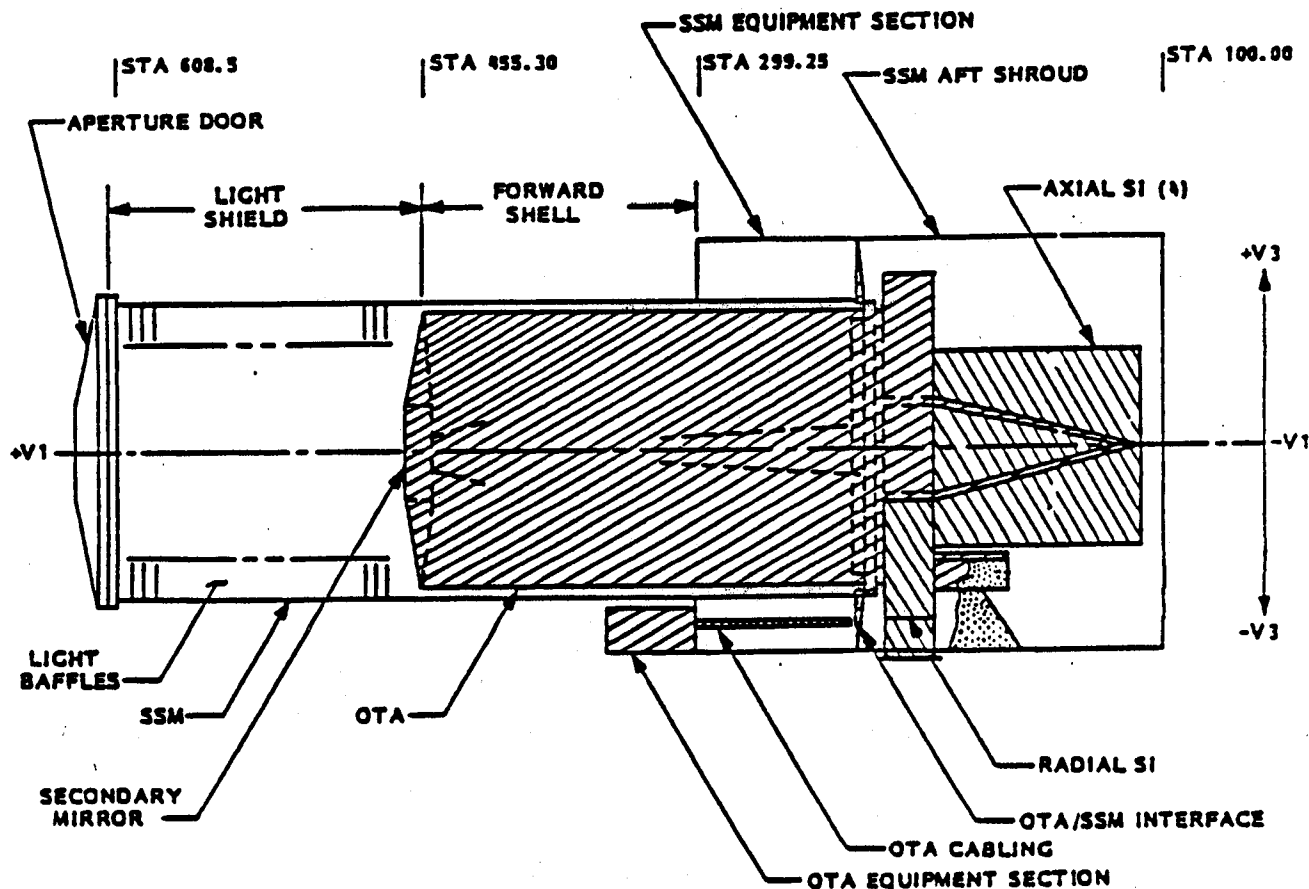Figure 1.3 Orbiter/ST Coordinate Relationships.

Figure 1.4 Support System Module—Design Features.

OTA Equipment Sections (ESs) with electrical equipment, Aft Shroud including Bulkhead (AS/AB), and Mechanisms.

1.3.2.2 Optical Telescope Assembly

The OTA (Figure 1.5) is the core of the ST and includes the 2.4-m, F/24, Ritchey-Chretian Cassegrain-type telescope. The OTA is composed of the following major components: Focal Plane Structure, Primary Mirror, Main Ring, Central Baffle, Main Baffle, Graphite Epoxy Metering Truss, Secondary Mirror Baffle, Secondary Mirror Assembly, and Equipment Section with electrical equipment.

Starlight travels through the aperture, down the assembly, and past the secondary mirror. The light then strikes the primary mirror where the beam is narrowed and is reflected to the secondary mirror where it is intensified into a small diameter beam. A meteoroid shield sun shade protects these optics. The beam passes through a 24-in. hole in the primary mirror to the focal plane almost five feet behind it. The focal plane is where the light originally captured by the primary is mirror turned into a focused image. Parts of the image enter the apertures of the SIs and are transmitted as data. The mirrors will be kept at nearly
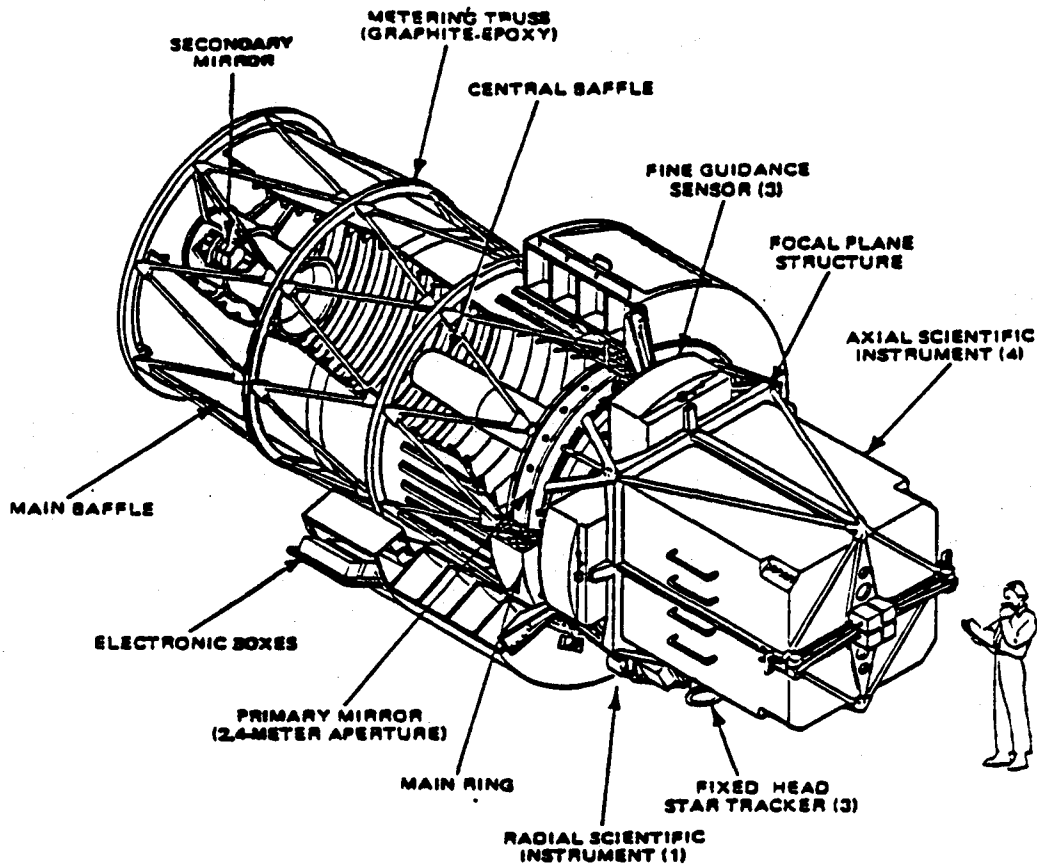
Figure 1.5 Optical Telescope Assembly—Design Features.

constant temperatures so that images at the focal plane wil not be distorted by changes in the environment. These images, as well as other SD, are converted to electronic digitized signals. The data are transmitted by means of high-gain antennas at a speed of up to one million bits per second.

1.3.2.3 Scientific Instruments (SIs)

The primary sources of information for General Observers on the science instruments are the Instrument Handbooks. The initial complement of SIs (Figure 1.6) includes two cameras, two spectrometers, and a photometer. The Faint Object Camera (FOC), Goddard High Resolution Spectrograph (GHRS), Faint Object Spectrograph (FOS), and the High Speed Photometer (HSP), are located in the axial position connected to the OTA Focal Plane structure (FPS). The Wide Field Planetary Camera (WF/PC) is a radial SI.

The FOC and the WF/PC are distinguished by their field of view, spatial resolution and wavelength range. Both instruments cover the ultraviolet and blue regions of the spectrum. The WF/PC also covers the red and near-infrared regions with a field at least 40 times larger than the FOC, but with a resolution degraded by a factor of two to four. The FOC has a
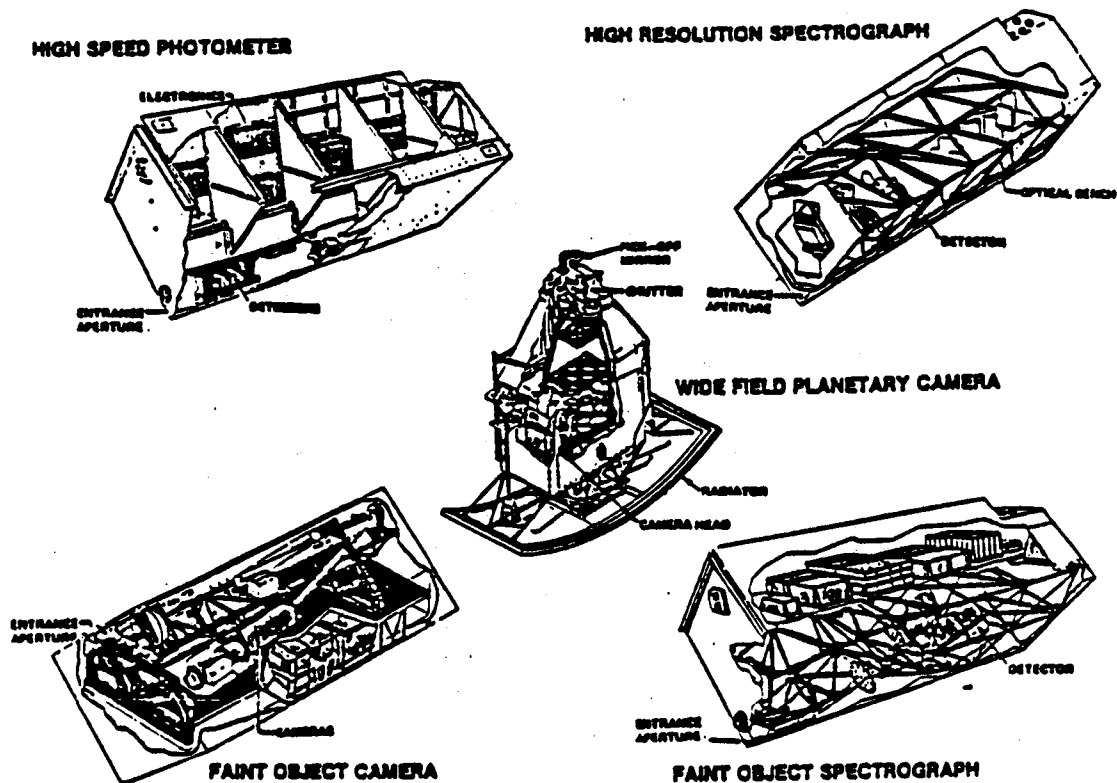
Figure 1.6 Scientific Instruments.

very small field of view but can use the highest spatial resolution which the ST optics can deliver.

The GHRS and the FOS provide a wide range of spectral resolutions which would be impossible to cover in a single instrument. Both instruments will record ultraviolet radiation. Only the FOS covers the visible and red regions of the spectrum.

The HSP is a relatively simple device capable of measuring rapid brightness variations over time intervals as short as 0.0001 sec. It can also be used to measure ultraviolet polarization and to calibrate other instruments.

1.3.2.4   SI Control and Data Handling (SI C&DH)

The SI C&DH (Figure 1.7) provides a unified command, data, and telemetry interface between the five SIs and the SSM Data Management System (DMA). The SI C&DH hardware is located in Bay 10 of the SSM Equipment Section and will provide the overall control of SI operations and data routing. The command software residing in the SI C&DH for each instrument will be reprogrammable, permitting modification of observing sequences as experience in the use of each instrument is gained. In addition, the instruments contain
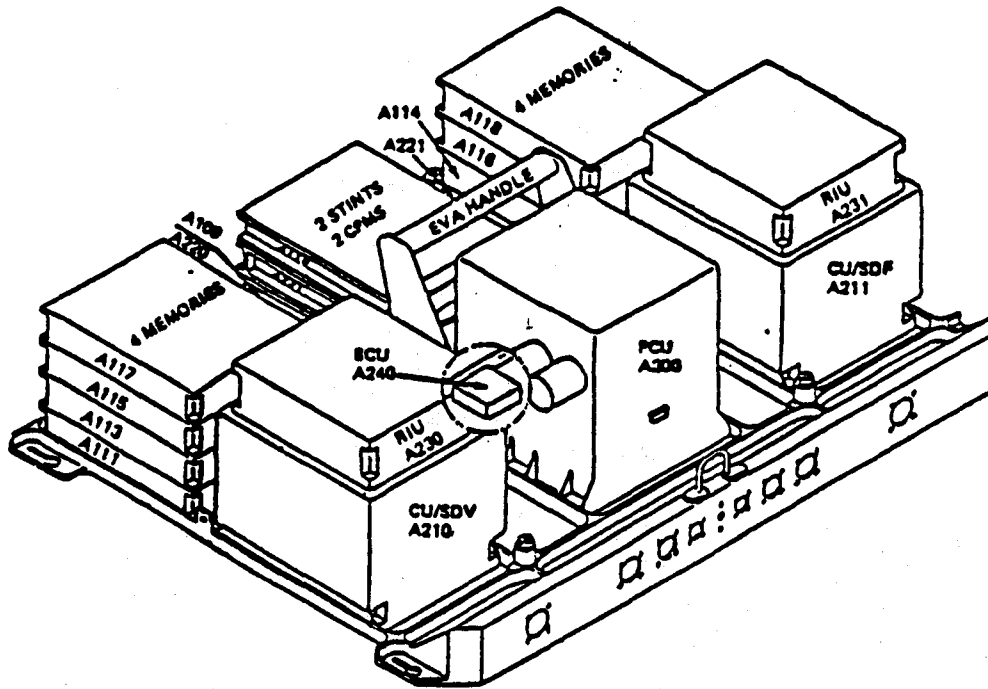
Figure 1.7 Scientific Instruments Control and Data Handling.

nonreprogrammable microprocessors that are used to implement internal sequences and data handling functions.

Major functions of the SI C&DH include the reception, decoding and storage of commands. Collected SI Engineering Data (ED) and Science Data (SD) is transmitted to the DMS. Other functions include: command storage, buffering, and formatting of SD into a transmission format, error correction coding of SD to provide a general computing capability to support SI control, monitoring, and data manipulation/analysis. The SI C&DH provides a power interface between the SIs and the SSM by conditioning power and providing for internal SI C&DH power distribution and redundancy selection.

The components of the SI C&DH illustrated above are: Control Unit/Science Data Formatter (CU/SDF), Multiplexed Data Bus (MDB), Bus Coupler Unit (BCU), Remote Module (RM), Standard Interface for Computer (STINT), NASA Standard Spacecraft Computer, Model I (NSSC-I), and Power Control Unit (PCU).

1.3.2.5 Solar Arrays (SAs)

The two SAs, shown in Figure 1.8, are affixed externally to the ST at the Forward Shell. Prior to deployment, each blanket is contained on a cylinder 15 in. in diameter. The cylinder is pivoted against the side of the telescope. Each SA will be unfurled when the ST is deployed and measures approximately 8 ft. by 40 ft. They provide at 2400 W average power to recharge the SSMs each time the ST completes the sunside portion of its 95-min orbit. The two SAs along with the batteries and power-conditioning equipment comprise the power supply system for the ST.
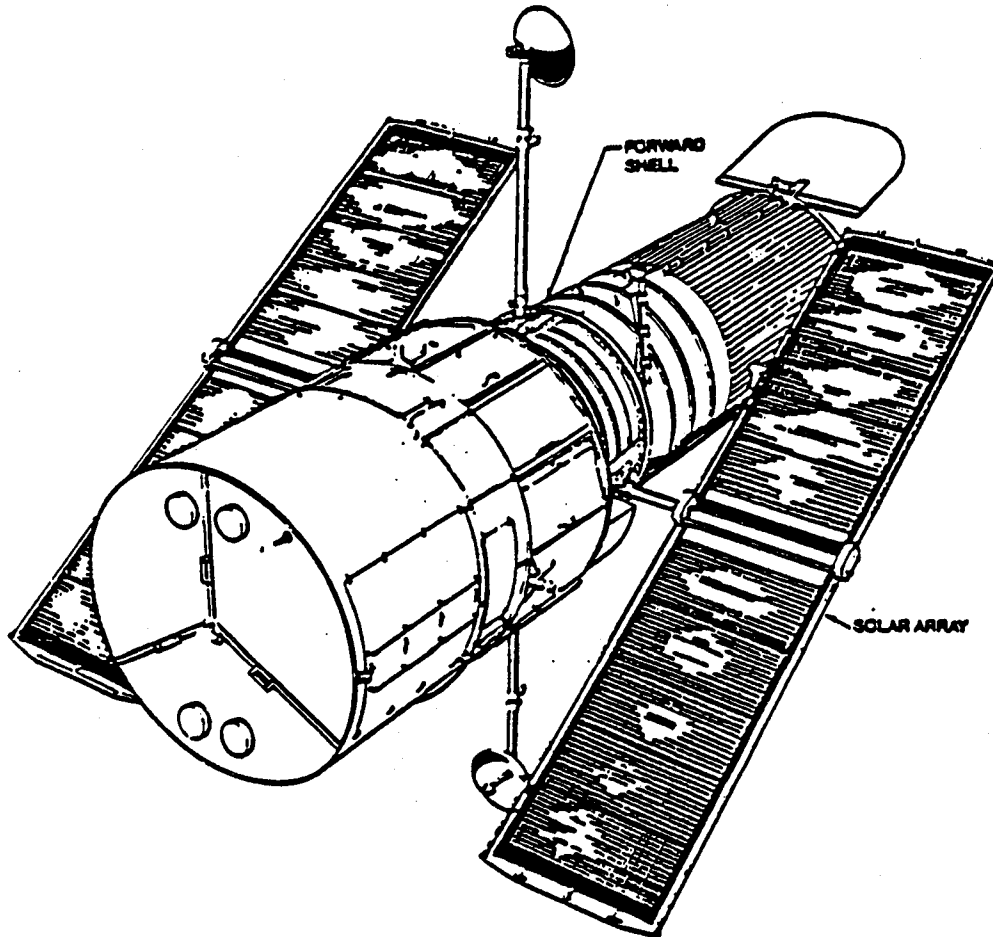
Figure 1.8 Space Telescope with Solar Arrays.

Each array is comprised of two flexible solar cell blankets, storage drum, and the necessary deployment/retraction and orientation mechanisms. An Electronic Control Assembly (ECA) is mounted in Bay 7 of the SSM equipment section and consists of the Deployment Control Electronics and the SA Drive Electronics. Electrical power is generated by the solar cell panels and then passed to the SSM EPS for conditioning and distribution. Power for all SA motors and instruments is controlled by the Electronics Control Assembly (ECA), which also accepts commands from the SSM and conditions data from the SA system for transmission to the SSM DMS and PSEA.

1.3.3   Mission Operation Ground System (MOGS)

The MOGS (Figure 1.9) consists of the Space Telescope Operations Control Center (STOCC) located at GSFC, Greenbelt, Maryland. STOCC is the major facility for the scheduling and control of ST operations. STOCC is composed of the Payload Operations Control Center (POCC) and the Science Support Center (SSC). POCC represents the focal point for all mission operations including HST command and control, determination of operating constraints and restrictions, HST health and status monitoring and contigency control of the HST. SSC represents the primary interface between the ST ScI and the POCC, including daily science scheduling, observer support, real time science operations, quick look data processing and display, and Scientific Data (SD) management. The SSC is the control point for science input and evaluation of SD. Also housed at GSFC is the ST Data Capture Facility (DCF) which receives SD from the ST and forwards it to the ST Science Institute (ST ScI) facility located at the Johns Hopkins University (JHU), Homewood Campus, Baltimore, Maryland.
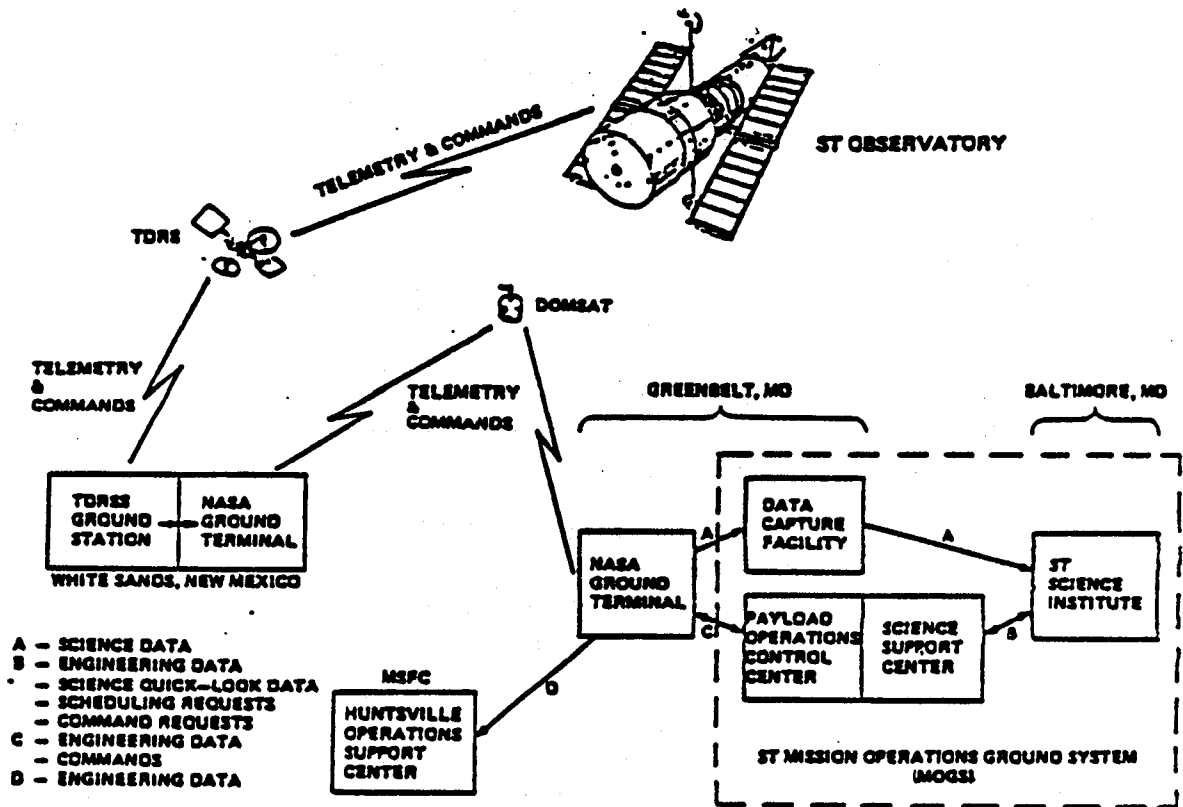

Figure 1.9 Mission Operation Ground System.

The ST ScI conducts an integrated ST science program including the establishment of observing policy, selection and support of ST observers, detailed science planning, observation implementation, and data archiving, processing and analysis. In addition to operations at its own location, the ST ScI povides scientists and other staff to perform operations at the SSC. The ST communication network (Figure 1.10) is described as follows: astronomers at the ST ScI, will decide where in the sky the ST should be pointed. Celestial coordinates are then transmitted via microwave link through the NASA Goddard Space Flight Center (GSFC), which is the Payload Operations Control Center (POCC). From the GSFC, the commands pass through a commercial communications satellite to a ground relay station at White Sands, New Mexico, transmitted to a Tracking and Data Relay Satellite (TDRS) in geostationary orbit, and thence to the ST. Digitized images and data are transmitted from the ST over the reverse path to the ST ScI.

1.3.4 Space Support Equipment (SSE)

The SSE is the mechanical and electrical hardware which aids the astronaut crew in deploying and retrieving the HST as well as performing Extra Vehicular Activity (EVA) during Maintenance Missions (MM).

The HST mounted crew aids permanantly mounted to the HST includes translation rails, handholds, tether loops, foot restraint receptacles, deployment umbilical, astronaut control panel, portable light receptacles, flight support system interfaces and micellaneous SI/changeout hardware.

The STS mounted SSE hardware is used in the deployment and retrieval of HST and will be returned to earth with each mission. This hardware consists of the umbilical disconnect mechanism. Interface Power Control Unit (IPCU), astronaut tools, the umbilical mounting bracket, tool mounting bracket, portable foot restraint, and jettison handle.

Section 9, provides a description of the Crew/Hardware Interface of the SSE during MM. Orbital Replacement Units (ORUs) approximate the size, weight, and HST location are listed and include Candidate ORUs (CORUs). Appendix A, Table A1-3 provides a listing of the SSE current weight values based on SSE Critical Work Element Audit Review (C-WEAR) data package. The SSE MM is briefly defined since a detailed description is beyond the scope of this handbook.

The Ground Support Equipment (GSE) is the mechanical and electrical hardware which are required for the installation, protection and operation of the HST prior to flight. These GSE are beyond the scope of this handbook. Other GSE such as communication hardware utilized during flight are defined briefly in Section 8 (Mission Operations Ground System).
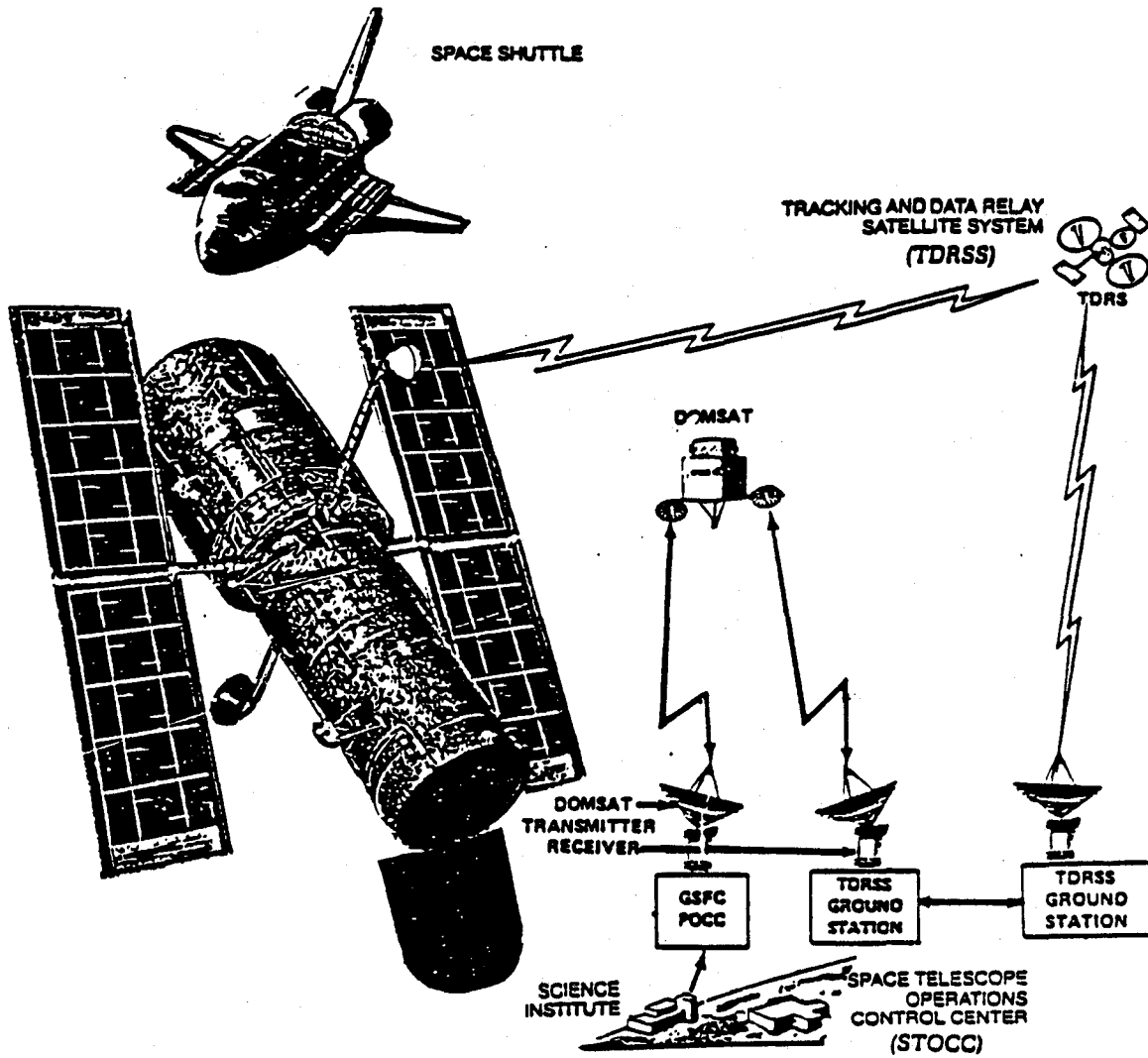
Figure 1.10 Space Telescope Communications Network.

2.0   FOCAL PLANE GEOMETRY

2.1   COORDINATE SYSTEMS

In subsection 1.3.1.3 the V1, V2, V3 coordinate system is defined relative to the space-craft. The cassegrain telescope inverts the image of the sky onto the focal plane. Hence, for example, FGS #2 is physically located in the +V3 direction relative to the OTA axis (it is on the sunlit side of the spacecraft) but it looks at a region of the sky that is further from the sun than the center of the telescope field of view.

Figures 2.1 and 2.2 show the physical V2, V3 coordinates of the apertures looking from behind and in front of the focal plane. Figure 2.3 shows the effect of projecting through the OTA onto the sky.
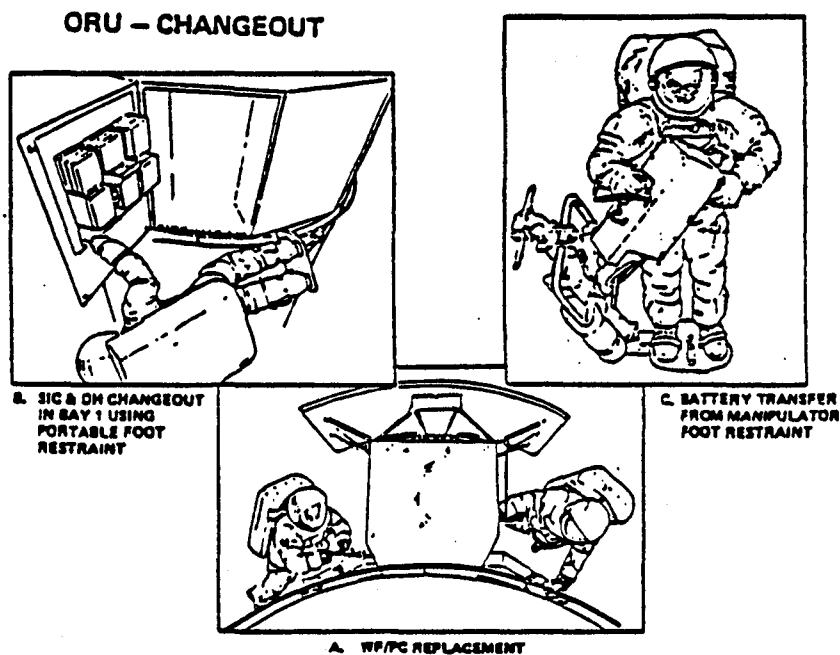
ORU – CHANGEOUT

Figure 1.11 ORU – Changeout.

2.2 OTA OPTICAL DESIGN

This section is taken from a Perkin-Elmer report. The telescope is an aplanatic Cassegrain configuration of the Ritchey-Chretian design as illustrated in Figure 2.1.

2.2.1 Prescription

The OTA optical design prescription is show in Table 2.1. The aspheric constant E is defined as:

$$E = 1 - \epsilon^2$$

where ϵ is eccentricity.
The sag of the aspheric surface is given by the following.

$$X = \frac{CS^2}{1 - (1 - E)C^2S^2}$$

where C = reciprocal of the vertex radius
S = radial distance perpendicualar to the optical axis.

U3

FGS 2

UV1

VIS

HRS   HSP

POL   UV2

1

2   4

U2   FGS 3   FGS 1

RED   f/288,
3   f/96

FOS   BLUE

FOC
f/48

10'

Figure 2.1 HST Focal Plane Layout (as seen from behind focal plane).

Figure 2.2 Hubble Space Telescope Axial Scientific Instrument.

Figure 2.3 FOV overlay placed with HSP VIS aperture plate on central star of PK 164+31°1, for $\theta_{opt} = 211°$.

Table 2.1
OTA Optical Design Prescription

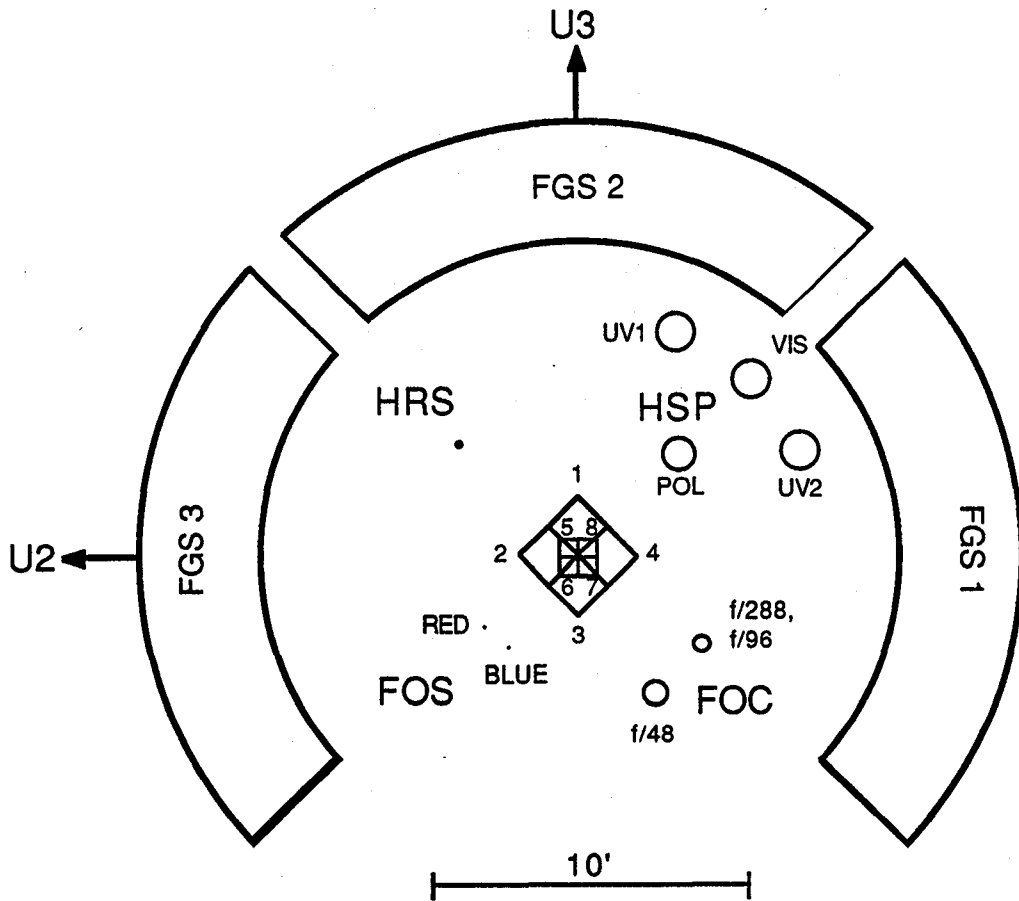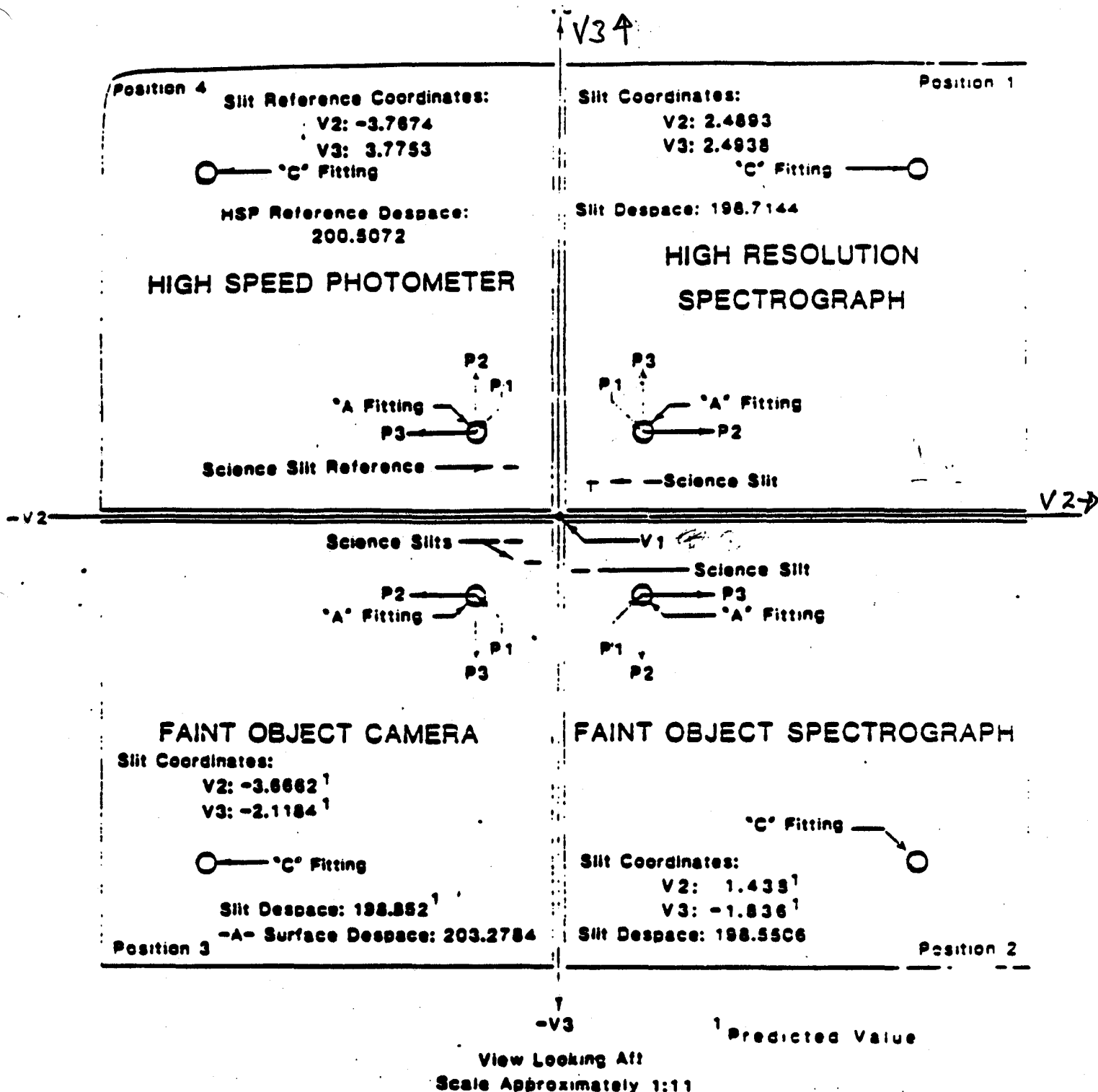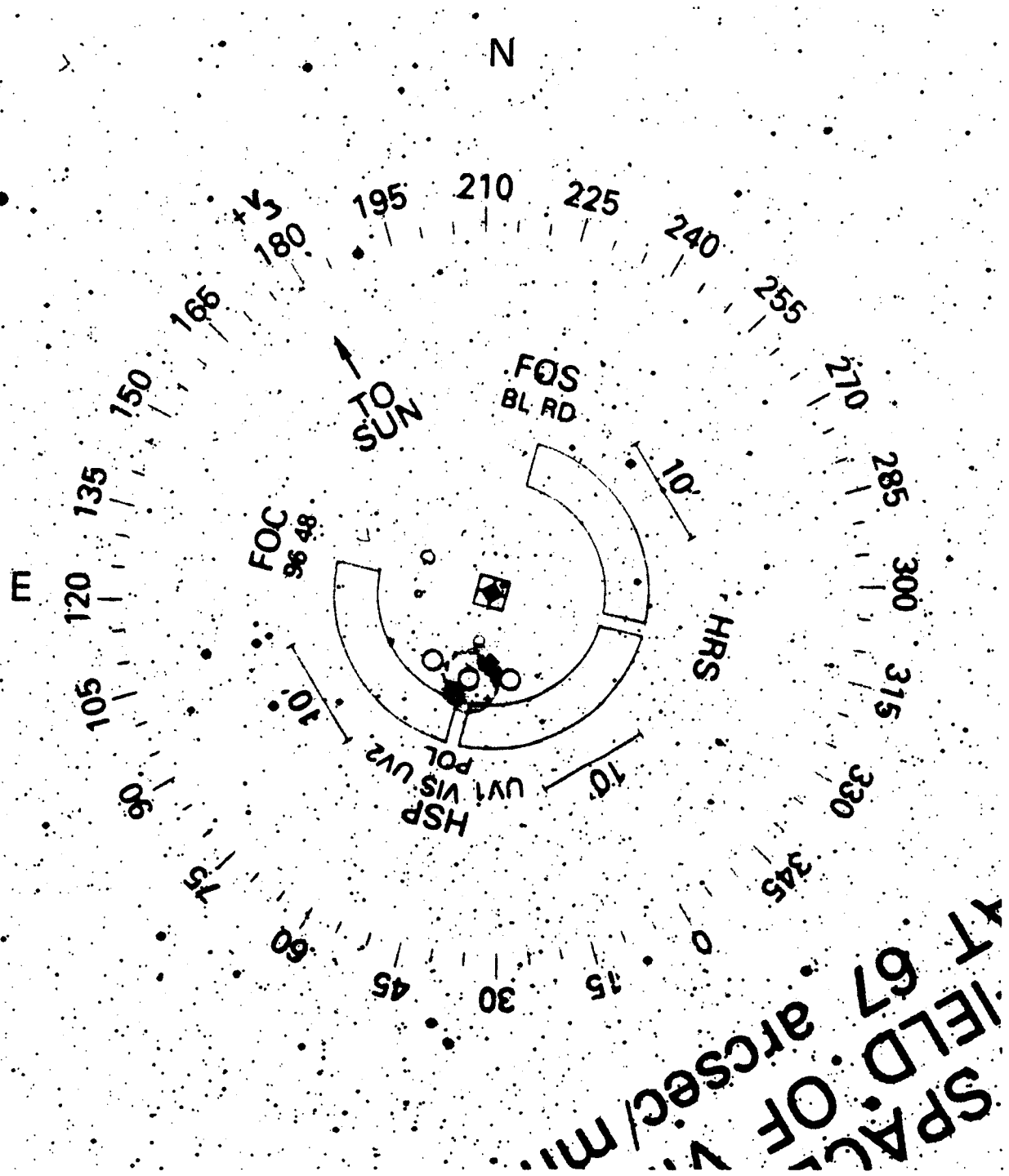| FORM	RITCHEY-CHRETIEN
Primary Mirror	
Radius	11040. mm
E	−0.0022985
Secondary Mirror	
Radius	1358. mm
E	−0.49686
Spacing	4906.071 mm
f/Number	24
Aperture	2400. mm
Vertex Back Focus	1500.129 mm
Back Focal Distance	6406.200 mm
Magnification	10.435
Exit pupil to focal plane	7003.51 mm

2.3.2   Performance Versus Field Angle

The OTA design aberrations are shown in Table 2.2. The design has no third-order spherical aberration or coma, with field curvature and astigmatism being the prime residual aberrations. As shown in Table 2.2, there are also very small amounts of residual fifth-order spherical aberrations and coma (distinguishable from third-order by field-angle dependence).

2.3   FOCAL PLANE DISTORTION

Given here are some fits to the HST focal plane. There are fits to the nominal focal plane (against which the SI were designed), and fits to the present best estimate of the focal plane (based on measured mirror radii). In the latter case we give the best focal plane as well as the tangential and saggital focal planes. The various SIs have apertures positioned nominally at one of the planes given here, as follows.

- The FOC F/96 and F/288 (internal focus adjustment possible): Apertures are positioned in the tangential focal plane. The relays correct the off-axis astigmatism.
- The FOC F/48 (internal focus adjustment possible): Should be in the best focal plane (for the spectrographic slit to work.)
- The WFC (focus adjustment possible): It is possible to use the Kelsall spots to fix the position of the pyramid edges on the CCD. The apparent position of an astrometric star field on the CCD in any relay then gives the (V2,V3) coordinates of the pyramid vertex.
- The PLC (focus adjustment possible): Same as WFC.
- The HSP (no focus adjustment): Should be positioned in the plane of best focus. Each aperture plate is flat, so apertures can only be there on average.
- The HRS (no focus adjustment): Needs to be close to the best focus.
- The FOS (no focus adjustment): Needs to be close to the best focus.
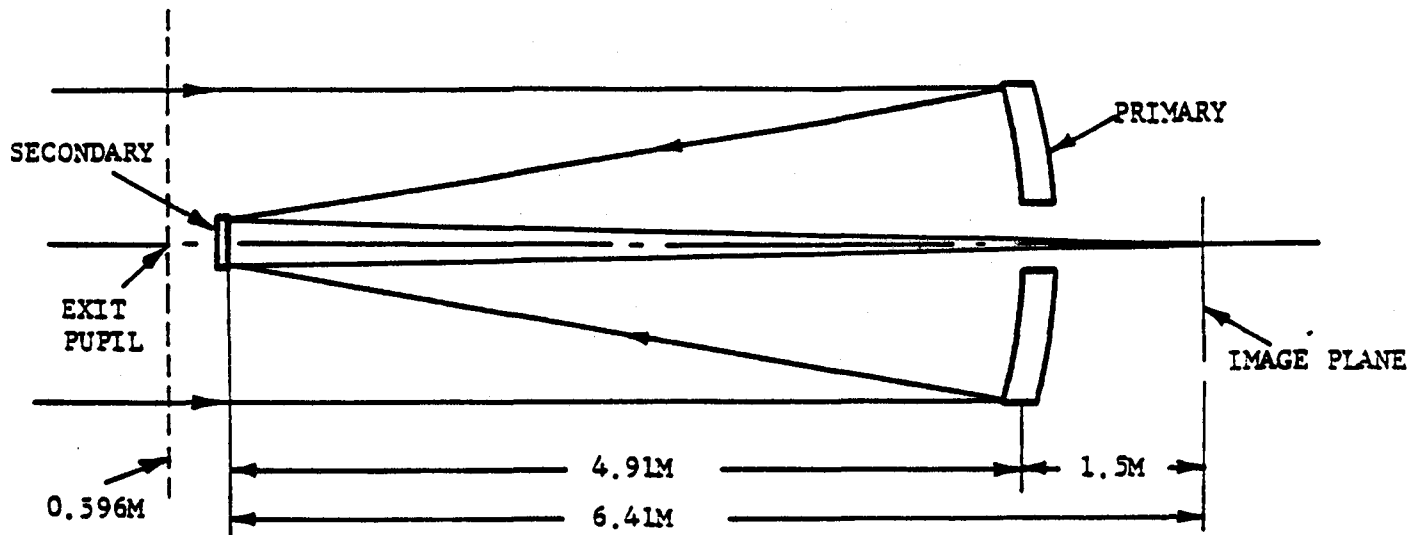
Figure 2.4 OTA Optical Design.

Table 2.2
OTA Design Aberrations

Longitudinal Aberration	Axis	7 Arc-Min	14 Arc-Min	Form
Field Curvature (mm)	0	−10.9	−43.5	h^2
Astigmatism (mm)	0	2.1	8.3	h^2
Wavefront Aberration				
RMS (λ)	0	0.148	0.594	
Spherical (λ)	0	−0.003	−0.0014	$h^2 r^4$
Coma (λ)	0	−0.011	−0.086	$h^3 r^3 \cos \theta$
Astigmatism (λ)	0	0.352	1.408	$h^2 r^2 \cos \theta$
($\lambda = 6328$Å)				

Ignoring pupil aberrations, the chief ray passes through the center of the exit pupil given in section 2.2 and the aperture. The intersection of this ray with the focal surface then gives the corresponding field angle via the fits given here.

Field θ (arcmin)	X (mm) $(-V1)$	Y (mm) $(\sqrt{V2^2 + V3^2})$	Radial PS (arcsec/mm)	Trans. PS (arcsec/mm)
0.0	0.00000	0.00000	3.58109	3.58109
1.0	−0.24397	16.75413	3.57992	3.58121
2.0	−0.97582	33.50496	3.57644	3.58156
3.0	−2.19529	50.24917	3.57066	3.58215
4.0	−3.90199	66.98345	3.56263	3.58297
5.0	−6.09536	83.70450	3.55240	3.58404
7.0	−11.93905	117.09365	3.52567	3.58687
9.0	−19.71868	150.39016	3.49119	3.59066
11.0	−29.42400	183.56755	3.44986	3.59540
13.0	−41.04219	216.59936	3.40268	3.60111
14.0	−47.56391	233.05239	3.37723	3.60433

$$X = -0.243981\theta^2 + 0.066737(\theta/10)^4 \pm 3.6 \ 10^{-4}$$
$$Y = 16.754686\theta - 0.5514611(\theta/10)^3 \pm 4.6 \ 10^{-3}$$

Table 2.3 Tangential Surface with Specified OTA Mirror Radii

Field θ (arcmin)	X (mm) $(-V1)$	Y (mm) $(\sqrt{V2^2 + V3^2})$	Radial PS (arcsec/mm)	Trans. PS (arcsec/mm)
0.0	0.00000	0.00000	3.58096	3.58096
1.0	−0.20207	16.75482	3.58021	3.58106
2.0	−0.80820	33.50688	3.57798	3.58135
3.0	−1.81815	50.25344	3.57426	3.58184
4.0	−3.23153	66.99175	3.56909	3.58253
5.0	−5.04780	83.71905	3.56249	3.58341
7.0	−9.88598	117.12964	3.54516	3.58577
9.0	−16.32514	150.46318	3.52266	3.58891
11.0	−24.35523	183.69768	3.49545	3.59285
13.0	−33.96367	216.81111	3.46407	3.59759
14.0	−39.35514	233.31556	3.44701	3.60026

$$X = -0.202076\theta^2 + 0.065518(\theta/10)^4 \pm 4.7 \ 10^{-4}$$
$$Y = 16.755275\theta - 0.4585616(\theta/10)^3 \pm 3.9 \ 10^{-3}$$

Table 2.4 Sagittal Surface with Specified OTA Mirror Radii

3.0 THROUGHPUT

Perkin-Elmer has supplied values for the OTA mirror efficiency. They need correction for dust, the HST aperture obscuration, microroughness scattering and diffraction on the HST aperture. The approach adopted here is to consider the first two effects and derive a

Field θ (arcmin)	X (mm) $(-V1)$	Y (mm) $(\sqrt{V2^2 + V3^2})$	Radial PS (arcsec/mm)	Trans. PS (arcsec/mm)
0.0	0.00000	0.00000	3.58022	3.58022
1.0	−0.24398	16.75819	3.57906	3.58034
2.0	−0.97583	33.51305	3.57558	3.58069
3.0	−2.19532	50.26125	3.56982	3.58129
4.0	−3.90204	66.99946	3.56181	3.58212
5.0	−6.09544	83.72434	3.55161	3.58319
7.0	−11.93923	117.12081	3.52495	3.58604
9.0	−19.71900	150.42401	3.49056	3.58985
11.0	−29.26477	183.11056	3.45000	3.59454
13.0	−41.04299	216.64402	3.40228	3.60037
14.0	−47.56488	233.09909	3.37688	3.60361

$$X = -0.243984\theta^2 + 0.066648(\theta/10)^4 \pm 5.3 \ 10^{-4}$$
$$Y = 16.758747\theta - 0.5551638(\theta/10)^3 \pm 1.0 \ 10^{-3}$$

Table 2.5 Tangential Surface with Measured OTA Mirror Radii

Field θ (arcmin)	X (mm) $(-V1)$	Y (mm) $(\sqrt{V2^2 + V3^2})$	Radial PS (arcsec/mm)	Trans. PS (arcsec/mm)
0.0	0.00000	0.00000	3.58023	3.58023
1.0	−0.20218	16.75827	3.57947	3.58032
2.0	−0.80864	33.51380	3.57723	3.58061
3.0	−1.81912	50.26388	3.57350	3.58110
4.0	−3.23321	67.00577	3.56831	3.58178
5.0	−5.05033	83.73673	3.56169	3.58266
7.0	−9.89047	117.15499	3.54431	3.58499
9.0	−16.33155	150.49680	3.52175	3.58811
11.0	−24.23073	183.24250	3.49494	3.59196
13.0	−33.97114	216.86373	3.46311	3.59672
14.0	−39.36172	233.37356	3.44605	3.59937

$$X = -0.202187\theta^2 + 0.069473(\theta/10)^4 \pm 3.9 \ 10^{-4}$$
$$Y = 16.758722\theta - 0.4550118(\theta/10)^3 \pm 9.5 \ 10^{-4}$$

Table 2.6 Sagittal Surface with Measured OTA Mirror Radii

total OTA throughput. The scattering and diffraction redistribute the energy in the focal plane, but do not lead to a loss in total throughput. Therefore their effects are computed when the corrections for different sized apertures are included.

Field θ (arcmin)	X (mm) $(-V1)$	Y (mm) $(\sqrt{V2^2 + V3^2})$	Radial PS (arcsec/mm)	Trans. PS (arcsec/mm)
0.0	0.00000	0.00000	3.58023	3.58023
1.0	−0.22306	16.75821	3.57928	3.58034
2.0	−0.89215	33.51339	3.57646	3.58066
3.0	−2.00704	50.26250	3.57176	3.58120
4.0	−3.56733	67.00253	3.56524	3.58195
5.0	−5.57246	83.73044	3.55692	3.58292
7.0	−10.91425	117.13779	3.53512	3.58552
9.0	−18.02479	150.46030	3.50689	3.58898
11.0	−26.74794	183.17647	3.47344	3.59325
13.0	−37.50894	216.75389	3.43388	3.59854
14.0	−43.46650	233.23639	3.41273	3.60149

$$X = -0.223064\theta^2 + 0.066119(\theta/10)^4 \pm 6.1 \ 10^{-5}$$
$$Y = 16.758712\theta - 0.5049494(\theta/10)^3 \pm 8.4 \ 10^{-4}$$

Table 2.7 Best Focal Surface with Measured OTA Mirror Radii

- The best measurement of the current dust contamination level is 3% of the total pupil area, on the primary and secondary mirrors. An additional 2% is expected before orbit, primarily from launch. We conservatively assume that the samples in P-E's measurements were clean. A given dust particle absorbs or scatters an amount of light equal to its surface area, and diffractively scatters an equal amount. The total throughput is therefore expected to be 90% of that for perfectly clean optics, in a wavelength independent manner. The scattering is to such large angles that the light can effectively be assumed lost for purposes of evaluating the throughput contribution, at least for all apertures less than tens of arcseconds. Significant degradation, particularly in the far UV can be expected if other contamination has taken place, but there is presently no indication of this. The FOC TV test did not extend below about 200 nm. The FOS and GHRS actually diverge below 140 nm but in opposite directions when the component product prediction is compared with the measurements.
- The total HST entrance pupil area is 45240 cm^2. Of this, 4930 cm^2 is covered by the secondary obscuration, and 1320 cm^2 by the primary mirror pad supports and secondary mirror spider supports. Thus the total clear aperture is 38990 cm^2, and the total proportion of incoming light that enters the pupil, but is not absorbed by pupil obscurations is 0.862.

Figure 3.1 is a graph of the OTA throughput obtained by multiplying the P-E curve by the two correction factors above. It represents the percentage of incident flux on a 2.4 m diameter circular aperture that reaches the focal plane, as a function of wavelength. This curve is the currently installed OTA throughput curve in CDBS. In addition, as explained below, explicit aperture dependent terms must be introduced in the OTA description for point sources.

In the UV, the throughput depends strongly on the aperture through which it is measured, due to small angle scattering by mirror surface irregularities. At long wavelengths, the aperture size also affects the throughput due to diffraction on the telescope pupil. Even in the case of the cameras, there is typically an effective software aperture used in deriving photometry, and detecting faint sources, thus the effective throughput depends on the aperture used (which will in turn be determined by signal to noise considerations). This is a large effect for the HST point spread function, which differs from typical ground based seeing images in being more sharply peaked, but with much more extensive wings. Therefore, routine calibration plans must consider it explicitly.

Figure 3.2 shows the losses at various apertures due to microroughness scattering and diffraction on the circularly symmetric part of the HST aperture for an on-axis object. It does not include off axis astigmatism, diffraction by the spiders and pads (which contribute a maximum possible loss of 3%), or effects such as diffraction at a focal plane mask causing light losses at any subsequent collimator. The first two effects can be modelled accurately by the TIM software, described in Chapter 5, and have been neglected here only for simplicity. The last effect has been the subject of separate measurements.

The proportion of the incident flux that does not pass through a circular aperture in the focal plane of projected **radius** θ at wavelength λ is

$$P = \frac{\lambda(1 - 2\pi\alpha k_{min}^{2-\beta}\lambda^{-2}/(2-\beta))}{\pi^2 a\theta(1-\epsilon)} + \frac{(2\pi)^{3-\beta}\alpha}{\lambda^{4-\beta}\theta^{\beta-2}(\beta-2)} + E$$

where the power spectrum of the wavefront errors caused by mirror microroughness is given as $\alpha k^{-\beta}$ for wavenumber $k > k_{min}$ and zero elsewhere, a is the primary mirror radius, ϵ is the obscuration ratio and E is an error term that arises because the above formula is only accurate in the limit of large θ and λ. The values $\alpha = 27100\,\mu m^4 cm^{-\beta}$, $\beta = 2.17$ and $k_{min} = 0.0524\,cm^{-1}$ are used. They are based on Perkin Elmer measurements of the primary and secondary mirror surface roughness. On orbit in SV, there is a specific OLT to measure the scattering profile more accurately. The results of that test will enable us to refine the fit functions given here.

The correction E is significant for HST, and has been estimated for $0.05'' < 2\theta < 1.25''$ by performing a full simulation of the expected scattering. The power-law power spectrum corresponds to a power law structure function, (this corresponds to the mirror surfaces being modelled as fractals) and the PSF can be numerically determined, even for large wavefront errors. A series of such simulations were performed, and the throughput errors were fit by least squares. The result is that for this range of θ,

$$P = \frac{2.60\lambda(1 - 0.0112/\lambda^{-2})}{\theta} + \frac{1.23}{\lambda^{1.83}\theta^{.17}} - \frac{0.00951\theta^{2.05}}{\lambda^{3.57}} - \frac{0.0145}{\lambda^{3.27}\theta^{0.274}} \qquad (2)$$

when θ is expressed in arcseconds, and λ is the wavelength in microns, the terms in Equation 1 have been evaluated numerically, and P is now expressed as a percentage.

The overall throughput is given in Figure 3.1 less an aperture dependent term illustrated in Figure 3.2, and given parametrically in Equation 2. Quantitative examples are given in Table 3.1. In the case of the HSP and spectrographs, astigmatism and diffraction at the instrument aperture will mean that further corrections must be applied, these will be

calibrated separately on orbit, and must be estimated by different methods before launch. The cameras need to explicitly allow for software aperture throughput in their calibration plans. The revised throughput values given here and aperture corrections are installed in CDBS. Finally, one should bypass these terms for extended sources (corresponding to an infinite aperture). These results replace those in the January 1986 ST ScI Newsletter, which did not explicitly consider different aperture sizes.

Diameter Arcsec	λ nm	Simulation %	Analytic %	Error 1 %	Error 2 %	Diff. %
0.050	100	76.3	137.3	0.1	61.6	−0.7
0.100	100	71.2	122.3	0.3	50.9	−0.2
0.200	100	65.4	108.8	1.3	42.1	0.0
0.300	100	60.9	101.6	3.0	37.7	0.0
0.400	100	56.5	96.8	5.4	34.9	0.0
0.800	100	34.8	86.0	22.4	28.8	0.0
0.050	200	39.1	46.3	0.0	6.4	0.8
0.100	200	32.9	38.2	0.0	5.3	0.0
0.200	200	28.1	32.5	0.1	4.4	−0.1
0.300	200	25.8	29.9	0.3	3.9	−0.1
0.400	200	24.2	28.2	0.5	3.6	−0.1
0.800	200	19.9	24.7	1.9	3.0	−0.1
1.200	200	16.1	22.9	4.3	2.7	−0.2
0.050	400	37.3	30.3	0.0	0.7	−7.7
0.100	400	18.1	19.4	0.0	0.5	0.7
0.200	400	12.8	13.5	0.0	0.5	0.2
0.300	400	10.7	11.3	0.0	0.4	0.1
0.400	400	9.6	10.1	0.0	0.4	0.1
0.800	400	7.5	8.0	0.2	0.3	0.1
1.200	400	6.5	7.2	0.4	0.3	0.0
0.050	800	44.5	43.9	0.0	0.1	−0.6
0.100	800	32.6	23.2	0.0	0.1	−9.5
0.200	800	12.0	12.6	0.0	0.0	0.6
0.300	800	10.0	9.1	0.0	0.0	−1.0
0.400	800	7.2	7.3	0.0	0.0	0.0
0.800	800	4.5	4.5	0.0	0.0	−0.1
1.200	800	3.5	3.5	0.0	0.0	−0.1

Table 3.1 Results from simulations, the corresponding analytical approximations, and the two terms from the fit to the error. The values given in the third column are percentage losses from the total energy reaching the focal plane. The last column gives the difference between the simulation result and the result of Equation 2.
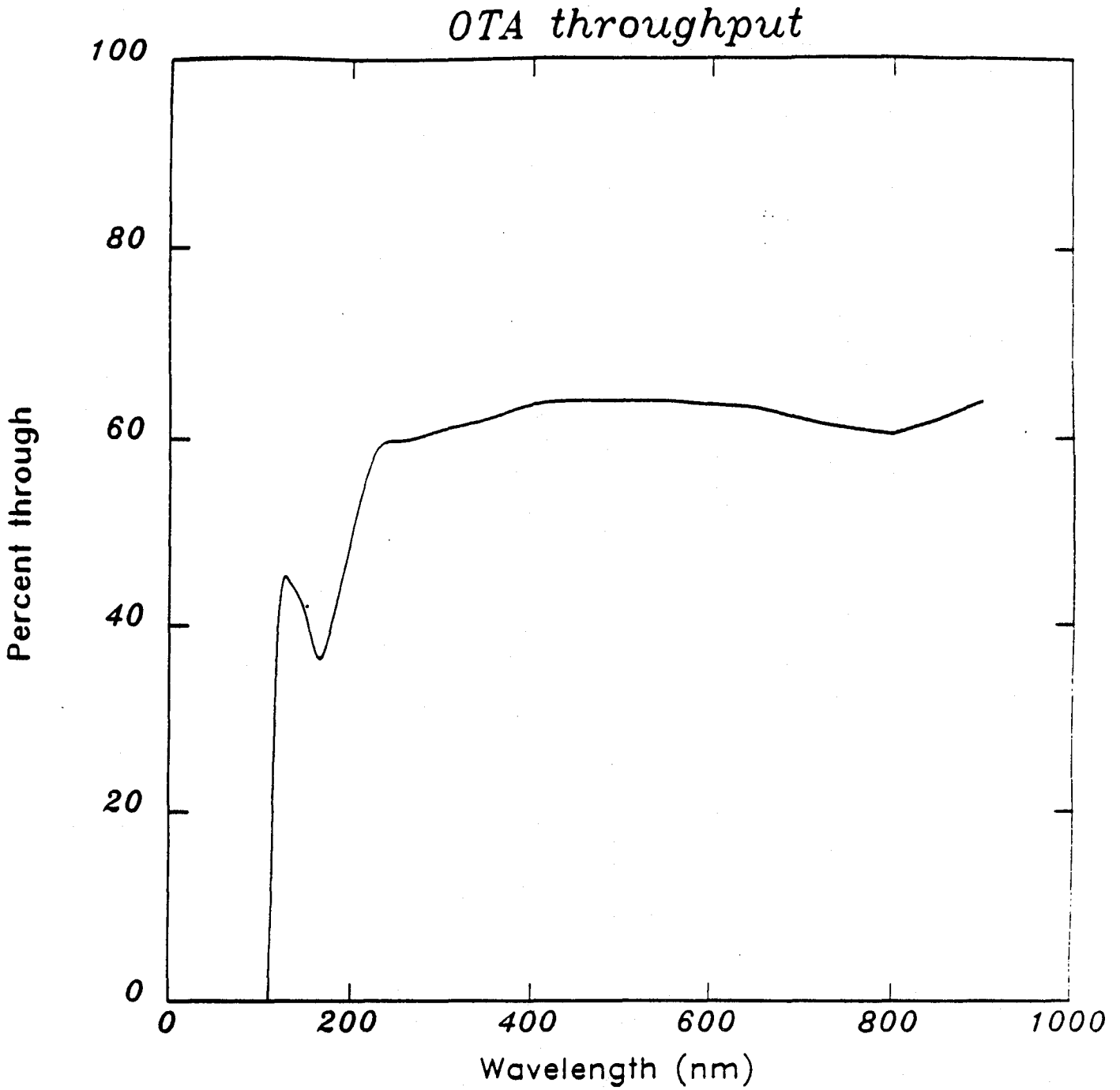
OTA throughput

Figure 3.1 Percentage of light passing a 2.4 m diameter clear aperture that reaches the OTA focal plane.
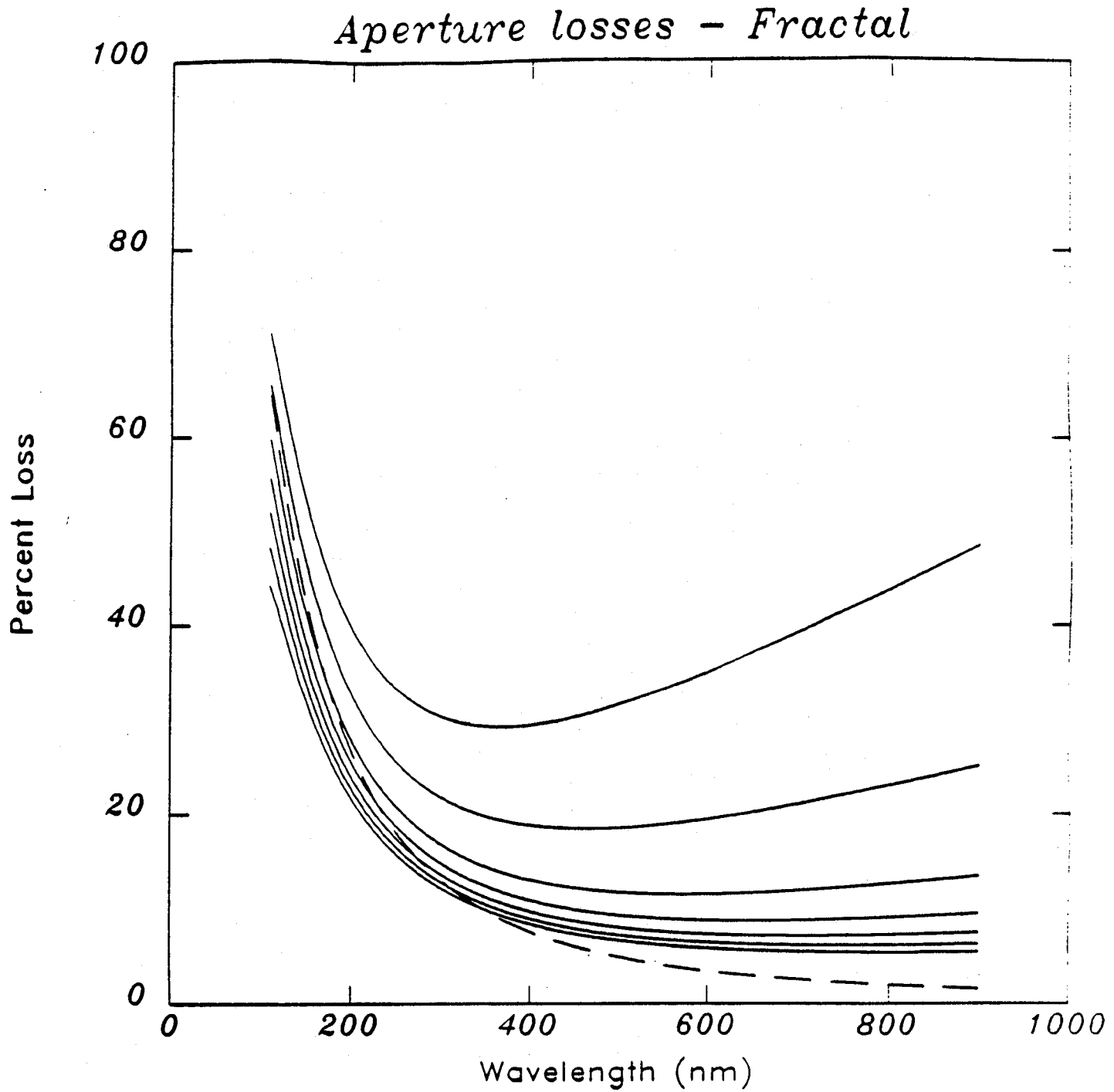
Figure 3.2 Percentage of light from a point source that passes outside centered apertures of diameters 0.1, 0.2, 0.4, 0.6, 0.8, 1.0, and 1.2″. Also shown is the loss given in the January 1986 ST ScI Newsletter.

4.0   POINT SPREAD FUNCTION

4.1   OVERVIEW AND SUMMARY

In this section, we enumerate the effects that change the PSF and give an overview of the appropriate models. These subjects are treated in more detail in section 4.2.

4.1.1   Large Scale Aberrations

The main large scale aberrations of the focal plane images are caused by three effects.

1. Design: The Ritchey-Chretien telescope in the case of the HST OTA has the primary and secondary aspheric coefficients chosen so that third order spherical aberration and coma are absent. However it does not eliminate astigmatism. This is the only third order aberration to affect image quality in the nominal design. An analytic expression exists for the magnitude of this aberration as a function of field angle (and is given in section 4.2.3). In the science instruments (SIs), this aberration is generally corrected, but residuals remain, and other aberrations are introduced by the design. Optical prescriptions for proprietary raytrace software can be used to produce an assessment of the design aberrations and serve to provide details of the described aberrations. Optical prescriptions are available for all the science instruments.

2. Manufacturing Errors: The mirror figures differ in radius, eccentricity and figure from the design. Full aperture interferograms of the primary and secondary mirrors have been analyzed to give the low frequency components of these errors as polynomials (the Zernike polynomials) over the aperture. Very little data is available on the manufacturing errors of the SI optics. The polynomial fits to the OTA errors are expected to be dominant.

3. Alignment and thermally induced errors: The position and orientation errors of the secondary with respect to the primary (despace, defocus and tilt) introduce further errors. The OCS provides for these parameters to be changed to minimize measured wavefront errors. However residual errors will remain (particularly because of desorption during the first years of the HST operation). Estimates of the RMS residuals for each Zernike polynomial have been made, and are included. The low frequency aberrations are described by the coefficients of Zernike polynomials. The polynomials and those associated coefficients are given in Tables 4.1–4.3.

4.1.2   Diffraction

The aberrations discussed in the previous section affect the image even in the geometric optics approximation. In a more complete wave description, diffraction becomes important, and indeed dominates the image size for ST. There are three components in the diffractive degradation of the image. The radius of the first airy ring is $\frac{1.22\lambda}{D}$ for an unobscured aperture. This is 53 milliarseconds for the HST aperture at 5000 Å.

1. The "design" diffraction caused by the entrance pupil. There are additional components due to the secondary baffle central obscuration, the secondary mirror spiders, and the primary mirror pads. It dominates the image for long wavelengths, and gives rise to the familiar Airy pattern of alternating dark and bright rings. Because the secondary obscuration is 0.33, the rings consist of a sequence of a brighter ring followed by two fainter rings, with the overall intensity falling as the inverse cube of the distance from

the center of the image. Superimposed on this pattern are spider diffraction spikes and a ripple effect caused by the pads. The dimensions of the entrance pupil are given in Figure 4.1.

2. The scattering caused by dust particles on the mirror and lens surfaces. The particles are typically ten microns across, and hence lead to a very wide diffractive scattering of the incoming light. Because they are randomly distributed over the surface of the mirror, their effects can be incoherently added and lead to an overall additive background in the focal plane near a bright source. Most of the energy is distributed over a region with projected diameter of 1°.

3. The scattering caused by mirror surface defects. The mirrors have aberrations at all spatial frequencies. The low frequency aberrations can be described as in the previous section, but the residual higher frequency errors can only usefully be described in a statistical manner. The ST primary mirror dominates this source of scattering because of the effects of the pupil magnification. Measurements are available of the full aperture residuals after the Zernike polynomial fits of the previous section, various subaperture positions on the primary, and very high frequency errors (FECO measurements). These measurements have been reduced to both a simple power spectrum and to autocorrelation functions. This source of diffractive scatter is expected to dominate the PSF in the UV. It is discussed in detail in section 4.3. Figure 4.2 shows the approximate regions of the θ-λ plane at which different effects dominate.

4.1.3   Jitter

If observations occurred instantaneously or the spacecraft were rigidly fixed in space the resulting image would be maximally sharp. However this is not the case, and some account needs to be taken of the movement of the optics. The dominant jitter is rigid movements of the field of view, caused by movement of the spacecraft as a whole. Image distortions caused by vibrations of the primary for example will be negligibly small. In fine lock the jitter is expected to have an amplitude of 7 mas RMS, for course track, estimates vary but something of order 20 mAS is expected.

4.2   DETAILED ERROR MODELS

4.2.1   Ray Tracing

Any optical system is defined by specifying
1. The positions, curvatures and refractive indices of each optical surface.
2. Aspheric coefficients, tilts and decenters if needed.
3. The aperture stops in the system. These define the entrance pupil and vignetting.
4. The field point(s) and wavelengths of interest.

This information is sufficient to define a suitable set of geometric rays and their paths through the system. Each ray originates on an object point (at infinity for HST), passes through the entrance pupil and is refracted and reflected as it passes through the system. The output from this stage of the analysis can be a spot diagram showing the distribution of ray intercepts with a given plane (usually chosen as the paraxial image plane). Many subsidiary results are also available.
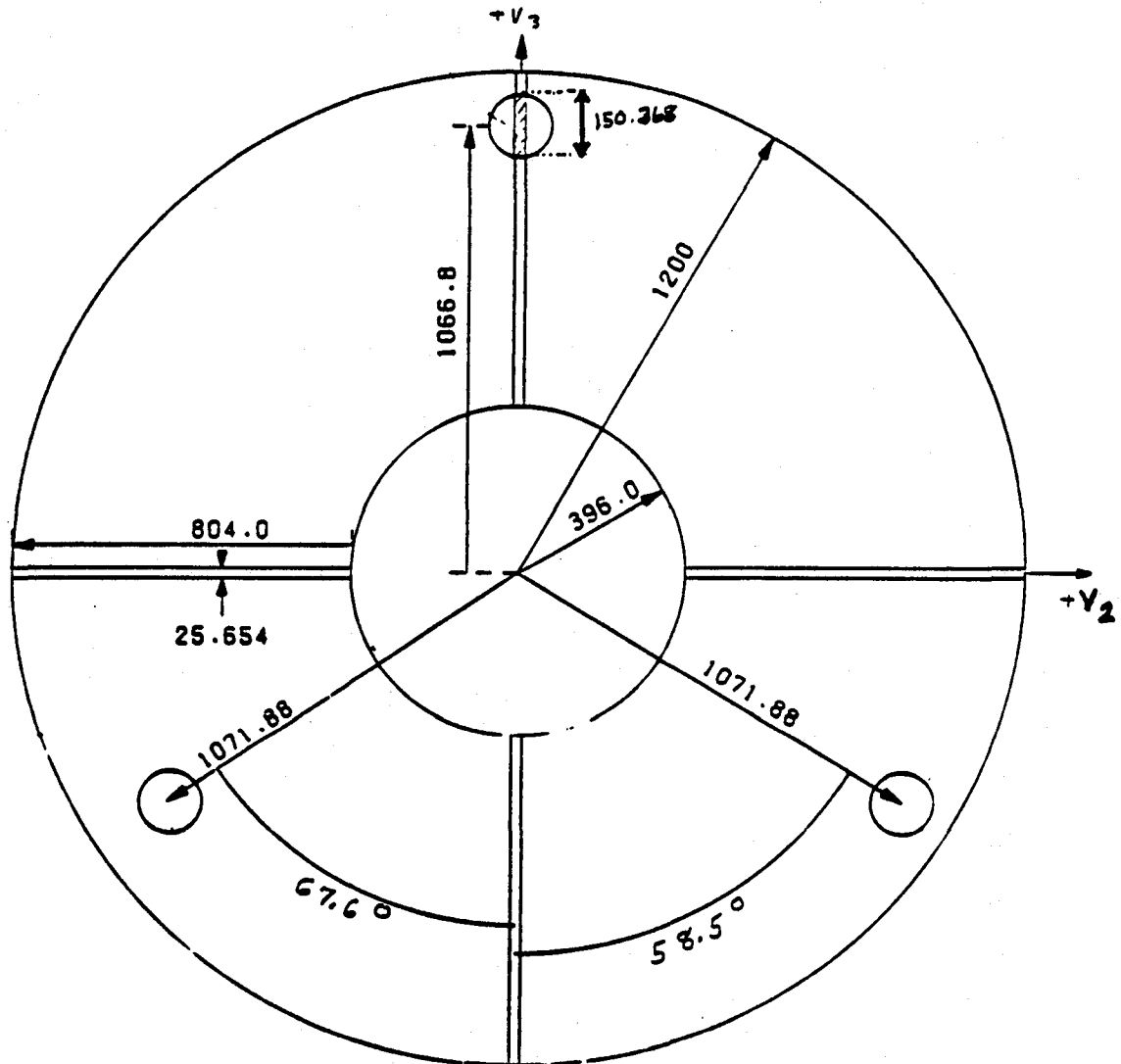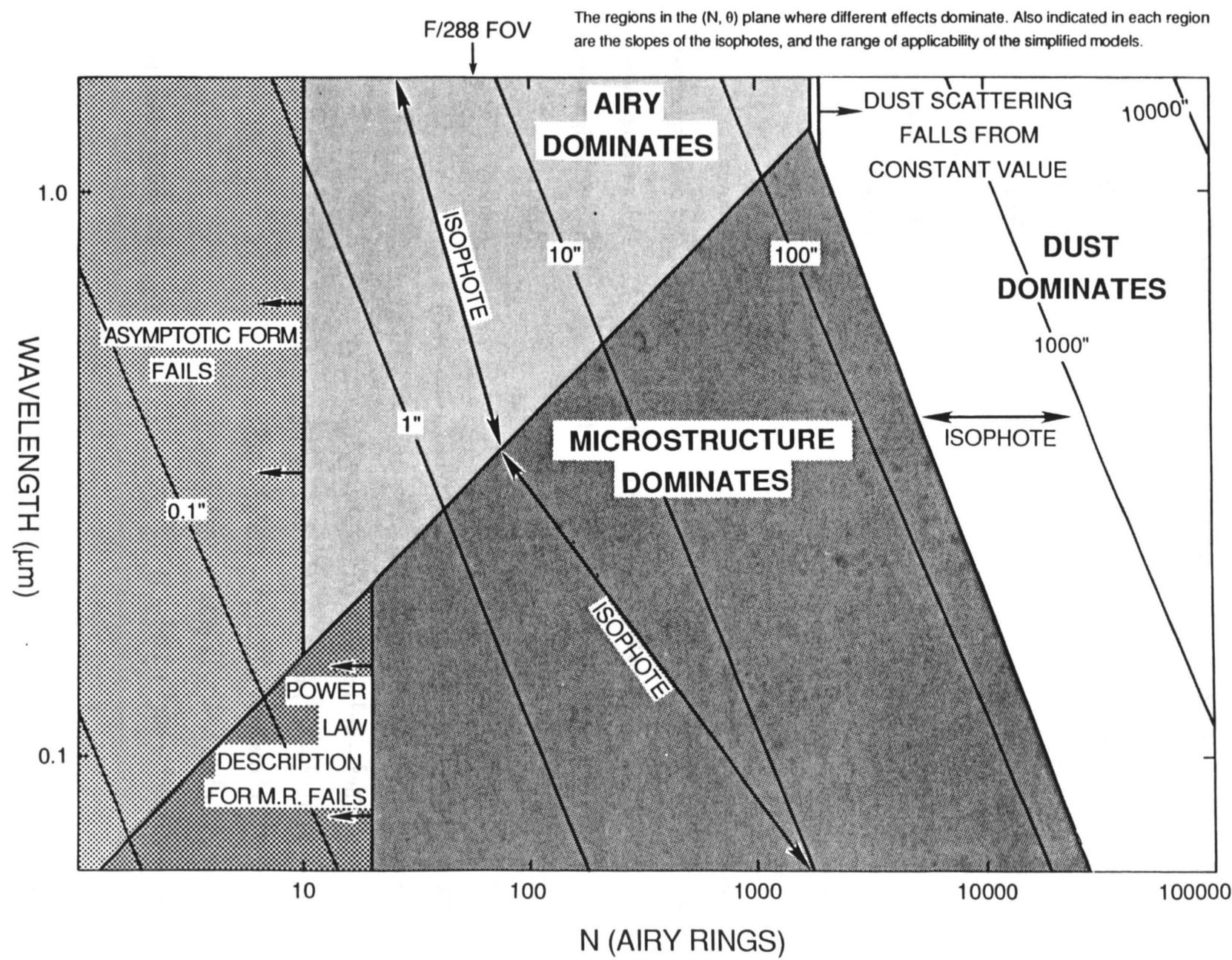
Figure 4.1 OTA Entrance Pupil.

The regions in the (N, θ) plane where different effects dominate. Also indicated in each region are the slopes of the isophotes, and the range of applicability of the simplified models.

Figure 4.2

Table 4.1. Zernike Polynomials for zero obscuration

$Z_1 = 1\theta$	Constant
$Z_2 = 2r\cos\theta = 2x$	X-tilt
$Z_3 = 2r\sin\theta = 2y$	Y-tilt
$Z_4 = \sqrt{3}(2r^2 - 1)$	Focus
$Z_5 = \sqrt{6}r^2\cos 2\theta = \sqrt{6}(x^2 - y^2)$	0° Astigmatism
$Z_6 = \sqrt{6}r^2\sin 2\theta = \sqrt{6}\,2xy$	45° Astigmatism
$Z_7 = \sqrt{8}(3r^3 - 2r)\cos\theta = \sqrt{8}x(3r^2 - 2)$	x-coma
$Z_8 = \sqrt{8}(3r^3 - 2r)\sin\theta = \sqrt{8y}(3r^2 - 2)$	y-coma
$Z_9 = \sqrt{8}\,r^3\cos 3\theta = \sqrt{8}x(x^2 - 3y^2)$	x-clover
$Z_{10} = \sqrt{8}\,r^3\sin 3\theta = \sqrt{8}\,y(3x^2 - y^2)$	y-clover
$Z_{11} = \sqrt{5}(6r^4 - 6r^2 + 1)$	3rd order spherical
$Z_{12} = \sqrt{10}(4r^4 - 3r^2)\cos 2\theta = \sqrt{10}\,(x^2 - y^2)(4r^2 - 3)$	Sphere astigmatism
$Z_{13} = \sqrt{10}\,(4r^4 - 3r^2)\sin 2\theta = \sqrt{10}\,2xy(4r^2 - 3)$	Sphere astigmatism
$Z_{14} = \sqrt{10}\,r^4\cos 4\theta = \sqrt{10}\,(x^4 - 6x^2y^2 + y^4)$	Ashtray
$Z_{15} = \sqrt{10}\,r^4\sin 4\theta = \sqrt{10}\,4xy(x^2 - y^2)$	Ashtray
$Z_{16} = \sqrt{12}(10r^3 - 12r^3 + 3r)\cos\theta = \sqrt{12}x(10r^4 - 12r^2 + 3)$	
$Z_{17} = \sqrt{12}(10r^3 - 12r^3 + 3r)\sin\theta = \sqrt{12}\,y(10r^4 - 12r^2 + 3)$	
$Z_{18} = \sqrt{12}(5r^3 - 4r^3)\cos 3\theta = \sqrt{12}\,x(x^2 - 3y^2)(5r^2 - 4)$	
$Z_{19} = \sqrt{12}(5r^3 - 4r^3)\sin 3\theta = \sqrt{12}\,y(3x^2 - y^2)(5r^2 - 4)$	
$Z_{20} = \sqrt{12}\,r^3\cos 5\theta = \sqrt{12}\,x(x^4 - 10x^2y^2 + 5y^2)$	
$Z_{21} = \sqrt{12}\,r^3\sin 5\theta = \sqrt{12}\,y(5x^4 - 10x^2y^2 + y^4)$	
$Z_{22} = \sqrt{7}(20r^6 - 30r^4 + 12r^2 - 1)$	5th order spherical

Table 4.2. Zernike Polynomials for 0.33 obscuration

Number	Normalization Factor	Polynomial
1	1.0000000	
2	1.8992573	$r \cos\theta$
3	1.8992573	$r \sin\theta$
4	3.8874443	$(r^2 - 0.554450)$
5	2.3137662	$r^2 \cos2\theta$
6	2.3137662	$r^2 \sin2\theta$
7	8.3345629	$(r^3 - 0.673796r) \cos\theta$
8	8.3345629	$(r^3 - 0.673796r) \sin\theta$
9	2.6701691	$r^3 \cos 3\theta$
10	2.6701691	$r^3 \sin 3\theta$
11	16.895979	$(r^4 - 1.108900\, r^2 + 0.241243)$
12	12.033645	$(r^4 - 0.750864\, r^2) \cos2\theta$
13	12.033645	$(r^4 - 0.750864\, r^2) \sin2\theta$
14	29.851527	$r^4 \cos4\theta$
15	29.851527	$r^4 \sin4\theta$
16	36.321412	$(r^5 - 1.230566\, r^3\ 0.323221\, r) \cos\theta$
17	36.321412	$(r^5 - 1.230566\, r^3\ 0.323221\, r) \sin\theta$
18	16.372202	$(r^5 - 0.800100\, r^3) \cos3\theta$
19	16.372202	$(r^5 - 0.800100\, r^3) \sin3\theta$
20	3.2700486	$r^5 \cos5\theta$
21	3.2700486	$r^5 \sin5\theta$
22	74.782446	$(r^6 - 1.663350\, r^4\ 0.803136\, r^2 - 0.104406)$
23	54.696500	$(r^6 - 1.340332\, r^4\ 0.405641\, r^2) \cos2\theta$
24	54.696500	$(r^6 - 1.340332\, r^4\ 0.405641\, r^2) \sin2\theta$
25	21.196833	$(r^6 - 0.833345\, r^4) \cos4\theta$
26	21.196833	$(r^6 - 0.833345\, r^4) \sin4\theta$
27	3.5320536	$r^6 \cos6\theta$
28	3.5320536	$r^6 \sin6\theta$
29	160.07455	$(r^7 - 1.781299\, r^5\ 0.948280\, r^3 - 0.142530\, r) \cos\theta$
30	160.07455	$(r^7 - 1.781299\, r^5\ 0.948280\, r^3 - 0.142530\, r) \sin\theta$
31	79.942692	$(r^7 - 1.429930\, r^5\ 0.477328\, r^3) \cos3\theta$

A commercially available software package CODEV (Optical Research Associates), which is capable of performing this function, has been selected and installed at the STScI. The SIs have each been described as suitable input files. The corresponding outputs have been generated for most cases and checked for consistency.

4.2 WAVEFRONT ERRORS

The optical path for a ray is defined as the sum of the products of the distances travelled with the corresponding refractive indices. The optical path difference (OPD) is the difference between the OP for the ray concerned from that of the chief ray. Given the results of a trace through the nominal system for a sufficient number of rays, it is possible to evaluate the magnitudes of all aberrations up to a desired order by the following procedure:

1. Evaluate the OPD at the exit pupil for a set of rays from a given object point.
2. Fit this set of points with the Zernike polynomials to the desired order.

The OPD $F(r,\theta)$ at any point (r,θ) may be expanded in terms of Zernike polynomials, $Z_{nm}(r,\theta)$ (where n is the order and m the degree of the polynomial), as:

$$F(r,\theta) = \sum_{n=1}^{N_{max}} \sum_{m=0}^{n} a_{nm} Z_{nm}(r,\theta) \tag{4.1}$$

The Zernike polynomials are of the form:

$$Z_{nm}(r,\theta) = R_n^m(r;\epsilon)\cos(m\theta) \; or \; R_n^m(r;\epsilon)\sin(m\theta) \tag{4.2}$$

where the radial polynomial $R_n^m(r;\epsilon)$ is a function of the central obscuration ϵ. (The twenty two Zernike polynomials used for $\epsilon = 0.$ and $\epsilon = 0.33$ are listed in Tables 4.1 and 4.2 respectively.)

Of particular interest are the lowest order terms in the expansion after image defocus and decenter have been removed. These give the tertiary spherical aberration, coma and astigmatism of the image. About 20 terms in the expansion are sufficient to fix the image quality for all practical purposes.

A library of Zernike coefficients are available for the SIs and OTA; on request.

4.2.3 Aberrated psf

The wavefront error at the exit pupil, together with the geometry thereof determine the PSF through the diffraction integral. This is in the form of the Fourier transform of the imaginary exponential of the OPD in waves over the exit pupil.

4.2.4 Mirror Surface Irregularities

The medium and high frequency primary mirror surface defects dominate the scattering due to mirror surface errors. They have been measured in full aperture, sub-aperture and FECO tests. There are two approaches to modelling the effect on image quality. One involves the use of the mirror autocorrelation function, and its effect on the MTF. This method was used by Perkin-Elmer and Dan Schroeder in their work on mirror scattering. The alternative involves the power spectrum and its effect on the PSF. It was used by Wetherell and Brown in their studies. The two approaches are not equivalent. They are described in detail in section 4.3.

4.2.5 Jitter

It is possible to regard the jitter as white noise in order to give a rough estimate of its effect. This corresponds to convolving the instrument PSF with a bi-Gaussian distribution to give the effective PSF. However this is not adequate if it contains frequency components close to or smaller than the inverse of the integration time. For example for very short exposures the optical axis will move with approximately constant velocity over the frame, and the effective PSF will be obtained by convolving the instrument PSF with a one-dimensional top-hat function. The effective PSF then becomes a function of the particular jitter generated during the observation, and ceases to be just a function of the average jitter power.

The effect of gaussian jitter of RMS amplitude J radians is to multiply the MTF by a frequency dependent degradation $\exp(-2\pi f^2 J^2 D^2)$. For HST in FGS fine lock J is expected to be about 7 milliarseconds. In coarse track it will be about 3 times bigger. These numbers should be compared to the image size given in section 4.1.2.

4.2.6 Dust Modelling

The effect on the PSF of wide angle scattering and absorption of light by dust particles present on the primary is negligible. More significant is the diffractive scattering caused by the many tiny obscurations in the pupil. The scattering amplitude is essentially constant out to the half-width of the diffraction pattern for the largest particle. Measured in Airy rings this is half the ratio of the primary mirror radius to that of the largest particle (about 100μ in diameter). In other words the scattering amplitude is essentially constant out to about the 2400th Airy ring. For one particle the proportion of the incident flux scattered is $\pi a^2/A$ for the entrance pupil of area A. Approximating Bessel function $J_1(x)$ by $x/2$ for small x and integrating over all sizes with $n(a)da$ per unit area gives

$$\frac{1}{I}\frac{dI}{d\omega} = \int_{a_{min}}^{a_{max}} \frac{\pi a^2}{A}\frac{\pi a^2}{\lambda^2} An(a)da. \tag{4.3}$$

The fractional area covered serves to normalize $n(a)$ and if a power law, $n(a) = qa^{-\xi}$, is used the expression can be evaluated . The correction to the PSF is additive.

$$(PSF)_{new} = (1 - 2f)(PSF)_{old} + P_0, \tag{4.4}$$

where $f \approx 5\%$ is the covering factor and P_0 is given by

$$P_0 = \frac{\pi f}{\lambda^2}\frac{3-\xi}{5-\xi}\frac{a_{max}^{5-\xi} - a_{min}^{5-\xi}}{a_{max}^{3-\xi} - a_{min}^{3-\xi}} \tag{4.5}$$

Here $\xi \approx 4.5$ is the dust power law exponent, $a_{max} \approx 100\mu$ is the radius of the largest dust particle and $a_{min} \approx 10\mu$ is the radius of the smallest dust particle.

4.2.7 Diffraction-Limited PSF

In the absence of aberrations and ignoring the pads and spiders, the image of a monochromatic point source in the focal plane corresponds to a normalized intensity distribution in the sky of

$$\frac{1}{I}\frac{dI}{d\Omega} = \frac{\pi r^2}{4\lambda^2(1-\epsilon^2)}\left|\frac{2J_1(x)}{x} - \epsilon^2\frac{2J_1(\epsilon x)}{\epsilon x}\right|^2 \tag{4.6}$$

where $x = 2\pi r\theta/\lambda$, and θ is the field angle from the source and r is the radius of the primary mirror.

In the presence of abberations the PSF can be expressed asymptotically as:

$$\frac{1}{I}\frac{dI}{d\Omega} = \frac{8r^2}{\lambda^2(1-\epsilon^2)x^3}(\cos^2(x - \frac{3\pi}{4} + F_A(1,\theta)) + \epsilon\cos^2(\epsilon x - \frac{3\pi}{4} + F_A(\epsilon,\theta))$$

$$- 2\sqrt{\epsilon}\cos(x - \frac{3\pi}{4} + F_A(1,\theta))\cos(\epsilon x - \frac{3\pi}{4} + F_A(\epsilon,\theta))\cos(F_S(1,\theta) - F_S(\epsilon,\theta)))$$

$$\tag{4.7}$$

where $F_{S(A)}$ are the symmetric and antisymmetric parts of the wavefront error. In the absence of abberations, this reduces to:

$$\frac{1}{I}\frac{dI}{d\Omega} = \frac{4r^2}{\lambda^2 x^3(1-\epsilon)}$$

after averaging over three airy rings, in the asymptotic wings of the profile. The central core has a FWHM of about λ/D radians.

4.2.8 Astigmatism

The radius of blur circle at best focus (no diffraction) TAC is

$$\text{TAC} = H^2Y(D - 2f)/(4Bf^2) \qquad = 4.3708 \times 10^{-7}\theta'^2 \text{ meters.}$$

where

D	= Mirror spacing	= 4.906 meters.
F	= Effective focal length	= 57.6 meters.
B	= D + Back focus	= 6.406 meters.
Y	= Semi aperture	= 1.2 meters.
H	= Image Height	$= F\theta'\left[\frac{\pi}{180\times60}\right]$ meters.

θ' = Field angle in arcminutes. $(0' < \theta < 14')$

For pure astigmatism the Optical Path Difference OPD is

$$\text{OPD} = -CH^2\rho^2\cos 2\phi.$$

where ρ = Normalized pupil co-ordinate $\epsilon \le p \le 1$ of ray.

ϕ = Azimuth of ray in pupil $0 \le \phi \le 2\pi$.

$$c = \text{Wavefront error on marginal sagittal ray at unit image height.}$$

The ray aberrations are (transverse).

$$TA_x = -\frac{MLc}{Y}2H^2\rho\sin\phi \qquad TAy = -\frac{MLc}{y}2H^2\rho\cos\phi$$

M = Angular magnification = 8.22
L = Distance from exit pupil to image = 7.00 meters = f/M
    TAC is the maximum transverse aberration, hence.

$$-cH^2 = \frac{TAC\,Y}{2F} = 4.552 \times 10^{-9}\theta'^2$$

Putting the OPD into waves at 633 nm gives.

$$\frac{OPD}{(\lambda = 633)} = \frac{4.552 \times 10^{-9}}{633 \times 10^{-9}}\theta'^2 p^2 \cos 2\phi = \frac{\theta'^2 p^2 \cos 2\phi}{139.06}$$

To get the RMS w/f error we observe that the mean of this function is zero, hence

$$\begin{aligned}
\text{RMS}^2 &= \int (OPD/\lambda)^2 \rho d\rho d\phi \bigg/ \int\int \rho d\rho d\phi \\
&= \left[\frac{\theta'^2}{139.06}\right]^2 \cdot \frac{\int_\epsilon^l \rho^5 d\rho}{\int_\epsilon^l \rho d\rho} \cdot \frac{\int_0^{2\pi}\cos^2 2\phi d\phi}{\int_0^{2\pi} d\phi} \\
&= \left[\frac{\theta'^2}{139.06}\right]^2 \cdot \frac{(1-\epsilon^6)/6}{(1-\epsilon^2)/2} \cdot \frac{1}{2} \\
&= \frac{1}{6}\left[\frac{\theta'^2}{139.06}\right]^2 (1+\epsilon^2+\epsilon^4)
\end{aligned}$$

Hence, the RMS w/f error in waves at 633 nm is $\frac{\theta'^2}{321.75}\frac{\lambda}{24.83}$ at the FOS entrance aperture for example.

4.3 THE ST MICROROUGHNESS POWER SPECTRUM, AND ITS EFFECT ON THE PSF

This section summarizes the documentation on ST mirror microroughness and derives various fits to the power spectrum. For completeness, it also indicates the effects of a given level of ripple on the Point Spread Function (PSF). After a critical review of the approaches used in the past to deriving a fit to the power spectrum, it gives a new approach based more directly on the observations, bypassing somewhat the previous discussion of the appropriate bandpasses to use for the various measurements. The conclusion is that the effect is probably two to four times more severe than previously published sources have indicated.

Finally, a brief comparison is made with ground-based coronographic observations. These measurements indicate that the ST mirror may not be as good as at least one ground based mirror at medium and high frequencies. Measurements of extended sources more than two arcseconds from bright sources, when contrast against the background of the brighter source

is a limiting factor will probably be better done from the ground. This observation will be relevant to coronographic modes as well as to direct imaging. Observations of surrounding galaxies of quasars, circumstellar disks, and so on need to be carefully considered and optimized before HST can confer unique advantages.

A specific observatory level test is planned early in the mission to measure the actual levels of scattered light in the wings of the PSF. Observations that require low levels should not be scheduled until the test results are known, and the feasability of the observation is demonstrated.

4.3.1 Documentation Summary

Care must be taken in reading the applicable documentation concerning the magnitude of the surface ripple in different frequency regions. Much of the problem is that often it is not clear if the authors are discussing Optical Path Differences (OPD - relative to the chief ray in the exit pupil) generally measured in waves at some fixed wavelength, or surface deviations on a mirror such as the primary relative to the smooth design conical figure. In the latter case, the errors are frequently and conventionally also measured in waves. The two measures differ by a factor of two, if we ignore the small ray deviations caused by the surface errors. Further points are that the primary mirror was measured both before and after coating, and that the results differ by a small amount, and one must be clear if the secondary mirror contributions are included. Finally, different sources have widely varying assessments of the applicable bandpasses for the metrology measurements.

To help in reading the documentation, the following should clarify the choices made in various references, and the information available.

1. D. Kenyon in a Perkin Elmer report (#ST-SE-2105) dated 13-April-1982, provides a series of tables that quantify the wavefront error expected based on the pre-coating metrology. He gives 0.0161, 0.010, and 0.0054 waves at 632.8nm of OPD induced by the primary mirror, in the full aperture residual, subaperture and FECO tests respectively. He also gives results for the secondary mirror, and an estimate of the errors. No estimates of the appropriate bandpasses are included in this report. A summary is provided in Table 4.3.

BANDPASS	Primary	Secondary	Total	Total/Primary
Full Aperture Residuals	0.0161	0.0104	0.0206	1.2795
Subaperture (Area Weighted)	0.0100	0.0088	0.0155	1.5500
FECO	0.0054	0.0041	0.0091	1.6852

Table 4.3. *The wavefront error in waves at 633 nm. The total errors quoted are the RSS of the primary and secondary contributions and the errors on them. Also given is the ratio of the total and primary contributions. In the graphs and tables when comparing results for the primary only with cases involving both mirrors, the average RMS ratio of 1.50 is used*

2. D. Kenyon and P. Duerig in a Perkin Elmer report (#ST-SE-350) dated 22-May-1984, give instead the post-coating metrology (when available) and deal with mirror surface errors. They give 0.00656, 0.00513, and 0.0027 waves at 632.8nm for the three frequency ranges. These numbers should be doubled to compare them with the pre-coating metrology given above. They do not give measurements for the secondary mirror. There are four problems with this report. First, the Hankel transform given in their Equation 6 is incorrect. The correct form is given in Equation 7 here. Second, they perform a least square fit to the measured autocorrelation functions but do not fit the curve at the origin. This leads to a small loss of total power. Third, when estimating the overall fit to the PSD, they perform a least squares fit to the LOG of the individual power spectra for each bandpass, giving about a factor of 2 error in the fit function. Finally, the bandpasses reproduced in Table 4.4 that they ascribe to each measurement are probably incorrect.

3. P. Glenn in Optical Engineering (Vol. 29 No. 9) in September 1986, appears to be referring in his section 3 to the mirror surface errors. He gives there 21.0A and 18.0A for the full residual, and sub-aperture tests. He has confirmed verbally that these values are in error. When multiplied by 2 and converted to waves, they are close to the values quoted for the post coating metrology above.

4. R. Brown and C. Burrows in an article submitted to Icarus, use the pre-coating metrology for the primary in the full aperture residual and subaperture ranges, combined with estimates of the secondary mirror contribution in these two regions. They have a total RMS OPD of 0.0206 and 0.0160 waves of OPD respectively, numbers obtained from the first reference above. The bandpass limits they use were approved by the ST project in a meeting at MSFC, and are given in Table 4.4. They use a lower limit for the primary microroughness cutoff wavenumber of either $K = 0.04cm^{-1}$ or $K = 0.075cm^{-1}$, corresponding to uncertainties about where the residual power is measured. By assuming a power law for the variation of microroughness with frequency, and fitting the two possible assumptions, they get $G(K) = \alpha K^{\beta}$ where $\alpha = 27100 \pm 7.5\%$ and $\beta = -2.17 \pm 1.8\%$, for G being the power spectral density of OPD in $microns^4$, and K measured in cm^{-1}.

5. D. Schroeder in a technical note entitled *An approach to scattered light*, uses the approach described above of ascribing the measurements to particular bandpasses, integrating and deriving an appropriate power law for the microroughness power spectrum. Instead of using the full aperture residual measurements, with subaperture data, he uses the sub-aperture and FECO data. He uses wavelength ranges of $100mm$ to $1mm$ and $1mm$ to $20\mu m$ respectively, obtained from Perkin-Elmer reports 237b and 243b. The RMS wavefront errors he derives are lower than the values in Table 4.3 because he takes the RMS of the PM and SM measurements without including uncertainties in the measurements. The result he gets is summarized in Table 4.4, a low result similar to the flawed result from Kenyon and Duerig, mainly because of the large bandpasses ascribed to the measurements.

6. The Kenyon and Duerig report can be used to provide an alternative estimate of the bandbasses involved in the various measurements. This is the new approach that we advocate here. They give estimated autocorrelation functions, (summarized in Table 4.9 and described in more detail later) and from these, the individual distributions of the measured power can be obtained. They are plotted in Figure 4.1. It should be clear

from the Figure that conservative bandpass estimates can be obtained by using the points where the curves cross (or become sensibly zero) as a first attempt. We assume that the secondary mirror power is similarly distributed. Then, using all three derived bandpasses, one can fit a power law in a least squares sense. This avoids rejecting either low or high frequency data. The resulting bandpasses and fit to the power spectrum is given in Table 4.4, in the row labelled "Crossing points". The result is very similar to that in Brown and Burrows, although the bandpasses do not agree well.

7. An alternative and possibly more realistic estimate of the bandpasses can be obtained by plotting the contributions to the integrals of the power spectra as a function of frequency, as in Figure 4.2. The curves are highly peaked, and their half widths provide estimates of the bandwidths, if the assumption of a power law spectrum is accurate. These bandpasses are narrower, but the power they contain is still made to be the same in the fit. The result is that the overall fit must contain about twice as much power as the previous case and is given in Table 4.4, in the row labelled "Half power points."

SOURCE	BANDPASSES						FIT	
	Full aperture		Subaperture		FECO		α	β
Kenyon and Duerig	.314	6.28	1.57	62.8	31.4	3140.	13900.	-2.419
Brown and Burrows	0.04-0.075	1.26	1.26	31.4	*314.*	*3140.*	27100.	-2.170
Schroeder			.628	62.8	62.8	3140.	14100.	-2.262
Crossing points	.0946	.906	.906	18.8	18.8	6080.	29700.	-2.365
Half power points	.169	.445	1.01	2.46	25.17	284.	66500.	-2.410

Table 4.4. *The power law fit functions and the associated bandpasses limits used in their derivation, as wavenumbers $(K = 2\pi/\Lambda)$ in cm^{-1}. The OPD power spectrum is given by $G(K) = \alpha K^{\beta}$ in $microns^4$. Unused but stated bandpasses are given in italics. (Kenyon and Duerig's fit to the PM roughness has been renormalized by 1.5 from Table 4.3.)*

Tables 4.5 to 4.6 underline some of the conclusions above. They give the power in waves of primary mirror microroughness in many of the bandpasses referred to above for all the candidate fits to the power spectrum.

- In Table 4.5, Kenyon and Duerig's bandpasses are used. Their fit (shown in **bold**) does not reproduce their measured total power (6.73, 5.07 and 2.69 as in the top of the last column), and their bandpasses do not include most of the power (4.67, 3.92 and 2.46 in the diagonal at the top of the table body).

- In Table 4.6 are the bandpasses given in Brown and Burrows. They fit 20.6/3. = 6.87, and 15.5/3 = 5.17 in the low and medium bandpasses. The slight disagreement is due to their uncertainty about the location of the residual power. These bandpasses do miss some of the power in the measurements, as can be seen from the top of the table body.

- In Table 4.7 are the bandpasses at the crossing points of the power spectra. The least squares fit was aiming at values (6.87, 5.17, 3.03) in the three bandpasses respectively. Almost all the power in the measurements is captured in these bandpasses, as can be seen from the top of the table body. The fit involves two parameters but is through three points. Even so, the residuals are small. This means that the choice of fit function
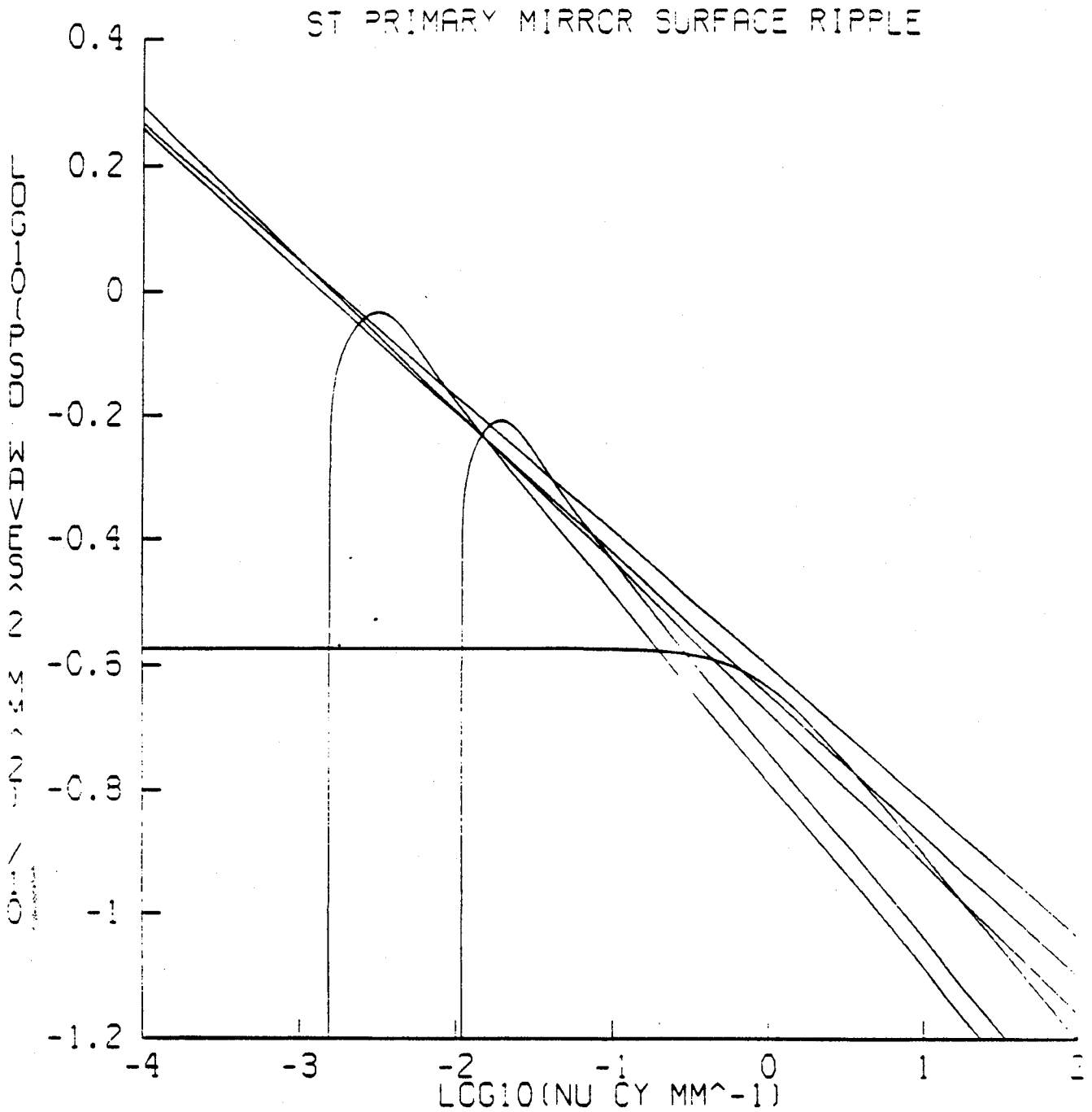
Figure 4.3 A plot of the mirror surface power spectra of various fit functions. ($\log_{10}$ PSD(waves^2 mm^2))/10. is plotted against $\log_{10} \nu(cy/mm)$. On the right of the graph, the upper straight line corresponds to the fit from Brown and Burrows, the middle one from Schroeder, and the lower one from Kenyon and Duerig. The three curves are the PM residual, subaperture and FECO measurements.
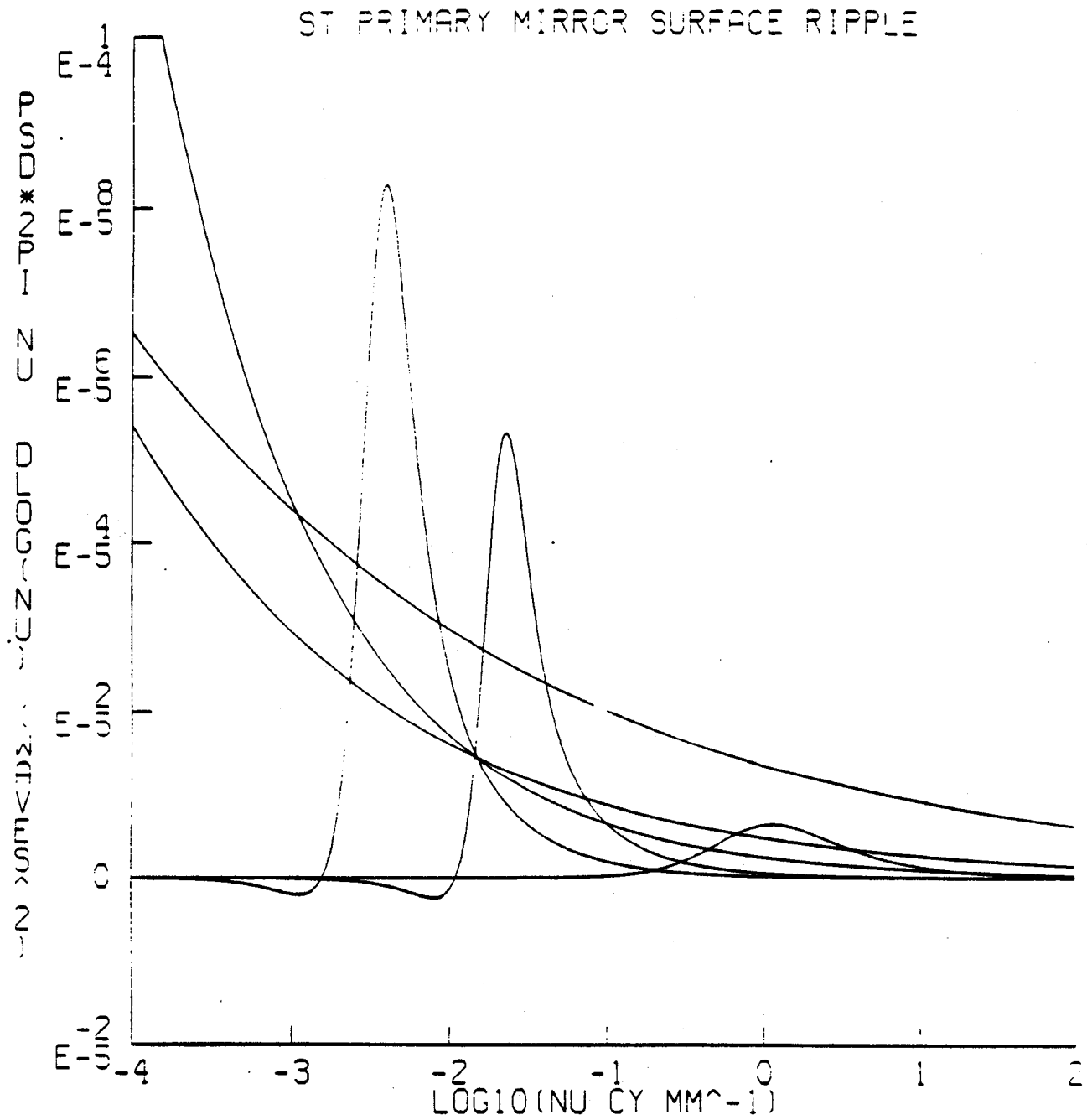
Figure 4.4 A plot of the contributions to the integrated total power (when integrating $d \log \nu$). Equal areas in the Figure correspond to equal power. The abscissae are in arbitrary units. The same cases as in Figure 4.1 are plotted. The half widths of the peaked curves for the different measurements provide a natural definition of the associated bandpass.

is consistent with the measurements. Alternatively, if one were to give zero weight to the FECO measurements for example, because of uncertainty about their bandpass, the fit would not be substantially different, and would predict about the right power in the assumed bandpass.

- In Table 4.8, the half power points were used to define the bandpasses. The least squares fit was aiming at identical values to the previous case. The majority of the power in the measurements is captured in these narrow bandpasses, as can be seen from the top of the table body. The same comments about the size of the residuals apply here as for the previous case. Thus, the last and most pessimistic microroughness fit in Table 4.4 may be the most accurate.

An important conclusion is that much previous work has underestimated the power by a factor of 2 to 4 and that even the choice made in Brown and Burrows is a conservative estimate of the effect.

	Low	Medium	High	Total
$K_{min}(cm^{-1})$	0.3142	1.5708	31.4159	0.0063
$K_{max}(cm^{-1})$	6.2832	62.8318	3141.5901	6283.1802
Full Aperture	4.6737	1.8370	0.4127	6.7310
Subaperture	4.8082	3.9220	0.7135	5.0759
FECO	0.2382	1.6516	2.4628	2.6892
Kenyon and Duerig	**4.1377**	**3.0895**	**1.7233**	11.0556
Brown and Burrows	5.8551	5.5041	4.6141	12.2697
Schroeder	4.1839	3.6064	2.5938	9.3263
Crossing points	6.0461	4.7428	2.8872	15.0448
Half power points	9.0409	6.8083	3.8552	23.8488

Table 4.5. *Powers in Kenyon and Duerig's defined bandpasses (horizontally) in thousandths of waves of primary mirror surface power for the various fit functions (vertically) defined in Tables 4.4 and 4.9. In this and subsequent tables, the last four rows have been renormalized by 1.5 in accordance with Table 4.3.*

4.3.2   Effects on the PSF

There are two approaches to modelling the effect on image quality. One involves the use of the mirror autocorrelation function, and its effect on the MTF. This method was used by Perkin-Elmer and Schroeder in some of their work on mirror scattering. The alternative involves the power spectrum and its effect on the PSF. It was used by Wetherell and Brown in their studies. The two approaches are not equivalent, except in the limit of very small ripple, and if corresponding autocorrelation functions and power spectra are used.

- In the first method the PSF in the absence of microroughness, PSF_0, is first computed as the modulus squared of the Amplitude Spread Function (ASF), obtained by a Fourier transform of the pupil function. An inverse Fourier transform gives the optical transfer

	Low	Medium	High	Total
$K_{min}(cm^{-1})$	0.0400	1.2600	314.0000	0.0063
$K_{max}(cm^{-1})$	1.2600	31.4000	3140.0000	6283.1802
Full Aperture	6.3997	2.0444	0.1240	6.7310
Subaperture	2.2629	4.4869	0.2141	5.0759
FECO	0.0482	1.0516	1.0136	2.6892
Kenyon and Duerig	6.5881	3.1387	0.9031	11.0556
Brown and Burrows	**7.3567**	**5.3332**	**2.9251**	12.2697
Schroeder	5.7351	3.5595	1.5388	9.3263
Crossing points	9.1366	4.7718	1.5821	15.0448
Half power points	14.2653	6.9051	2.0362	23.8488

Table 4.6. *Powers in Brown and Burrows' defined bandpasses (horizontally) in thousandths of waves of primary mirror surface power for the various fit functions (vertically) defined in Tables 4.4 and 4.9.*

	Low	Medium	High	Total
$K_{min}(cm^{-1})$	0.0946	0.9059	18.8287	0.0063
$K_{max}(cm^{-1})$	0.9059	18.8287	6083.8638	6283.1802
Full Aperture	6.2545	2.4293	0.5350	6.7310
Subaperture	0.7998	4.9262	0.9259	5.0759
FECO	0.0344	0.6799	2.6012	2.6892
Kenyon and Duerig	4.9057	3.3179	1.9806	11.0556
Brown and Burrows	5.7818	5.3672	5.1736	12.2697
Schroeder	4.4265	3.6493	2.9265	9.3263
Crossing points	**6.8935**	**4.9916**	**3.2938**	15.0448
Half power points	10.6470	7.2863	4.4249	23.8488

Table 4.7. *Powers in Crossing point defined bandpasses (horizontally) in thousandths of waves of primary mirror surface power for the various fit functions (vertically) defined in Tables 4.4 and 4.9.*

function (OTF) which is then multiplied by a frequency dependent degradation $M(f)$ defined as:

$$M(f) = \exp[-k^2\sigma^2(1 - c(2aF\lambda f))] \tag{1}$$

where $k = 2\pi/\lambda$ is the wavenumber of the light, σ is the RMS wavefront error, f is the spatial frequency in the image $(0 \leq f \leq 1/F\lambda)$ and $c(r) \equiv g(r)/\sigma^2$ is the mirror surface autocovariance function, which is only nonzero when r is less than the pupil diameter $2a$. A Fourier transform then yields the expectation value of the PSF in the presence of the ripple. This formulation can be shown to be exact for surface errors with a Gaussian distribution, or for small surface errors $(k\sigma \ll 1)$. Physically, a shift

	Low	Medium	High	Total
$K_{min}(cm^{-1})$	0.1691	1.0141	25.1756	0.0063
$K_{max}(cm^{-1})$	0.4453	2.4642	283.3932	6283.1802
Full Aperture	5.2603	1.8139	0.4423	6.7310
Subaperture	0.0000	4.0069	0.7649	5.0759
FECO	0.0158	0.0852	2.2900	2.6892
Kenyon and Duerig	3.2084	2.1284	1.5585	11.0556
Brown and Burrows	3.7995	3.1326	3.7059	12.2697
Schroeder	2.9073	2.2113	2.1861	9.3263
Crossing points	4.5172	3.1422	2.5520	15.0448
Half power points	**6.9659**	**4.6591**	**3.4732**	23.8488

Table 4.8. *Powers in half power defined bandpasses (horizontally) in thousandths of waves of primary mirror surface power for the various fit functions (vertically) defined in Tables 4.4 and 4.9.*

of one pupil diameter in the autocorrelation of the wavefront corresponds to the cutoff frequency of the optical system. Smaller shifts correspond to proportionately smaller spatial frequencies in the image.

- When $k\sigma \ll 1$, we can expand the second half of the exponential (involving $c(r)$) in Equation 1. The first term in the expansion gives a term proportional to PSF_0 after a Fourier transform. The second transforms to a convolution of PSF_0 and the transform of the autocovariance function, i.e. the power spectrum. PSF_0 is essentially a delta function relative to the spread of the power spectrum, and the end result is

$$\frac{1}{I}\frac{dI}{d\omega} = \exp(-k^2\sigma^2)PSF_0 + \frac{4\pi^2}{\lambda^4}G(2\pi\theta/\lambda) \qquad (2)$$

where $G(K)$ is the power spectral density for the wavefront errors. The scattering from a grating with frequency M cycles per pupil has a first order diffraction peak at Airy ring number M. Higher (neglected) terms in the expansion performed above correspond to higher diffraction orders. This provides a physical insight into the meaning of the formulation.

The above formulations give theoretical predictions of the effects of given levels of ripple on the PSF. As inputs, they require analytical or numerical approximations to the power spectrum or autocorrelation function. Several different approaches have been used and they are summarized here, with a discussion of their limits of applicability.

- The simplest approach is to use the power spectrum formulation, together with a fit such as those in Table 4.4. Then, the power spectrum is represented as

$$G(K) = \alpha K^\beta, \qquad (3)$$

where β is the power law exponent and α is related to the RMS microroughness δ_e^2 in a given bandpass through the relation

$$\delta_e^2 = \frac{1}{2\pi} \int_{K_1}^{K_2} K G(K) dK = \frac{\alpha(K_2^{\beta+2} - K_1^{\beta+2})}{2\pi(\beta+2)} \tag{4}$$

This approach has the advantage of being well behaved at large angles. It does have disadvantages. First, below about 20 cycles per pupil, *i.e.*, within the first 20 rings, the fit to the power spectrum breaks down. Indeed it is singular at the origin. It does not correspond to any particular function in transform space because of this singularity. In practice, when using Equation 2 the function is added to the renormalized PSF_0 only in its domain of applicability. The effect is that at short wavelengths, a discontinuity in the PSF becomes apparent when the microroughness contribution is comparable or greater than the other component at the inner radius of its applicability. At longer wavelengths, the central component swamps the microroughness contribution at this point, and no discontinuity is evident. In the wings, even at the long wavelengths, the microroughness will dominate eventually because it falls as θ^β which is slower than the θ^{-3} characteristic of Airy diffraction. In addition, for ST in the UV, the condition $K\sigma \ll 1$ breaks down and while corrections to the total scattering can be calculated, the detailed distribution of the scattered light is uncertain.

- Schroeder has modelled the effects of the microroughness by parameterizing the autocovariance functions for various bandpasses.[1]

$$c(r) = \begin{cases} (1 - (r/r_{cut})^{1.5}) & \text{if } r < r_{cut} \\ 0 & \text{otherwise} \end{cases} \tag{5}$$

r_{cut} being a cutoff shift ($2a/18$ for medium frequencies and $2a/360$ for high frequencies.) If **both** medium and high frequency errors need to be modelled, the product of the appropriate MTF expressions is taken. This approach overcomes the deficiencies of the previous approach in the close field, and provides good results into the far UV. Unfortunately, it fails at large angles. The form chosen for the autocorrelation function contains a discontinuity in its derivatives, and this leads to unphysical oscillations in the corresponding power spectrum at high frequencies. These are reflected as ripples at large distances in the point spread function. Indeed, as the associated power spectrum is not constrained to be positive definite, and contains negative components, the PSF in the far wings can even appear negative. It can be seen that this approach complements almost perfectly the previous description of the power spectrum. It works best at small angles, the other best at large angles.

- The above two functional forms suffer in not being analytically transformable. Kenyon and Duerig use fits to the measured autocorrelation functions of the form

$$g(r) = A\cos(Br)\exp(-Cr) \tag{6}$$

---

[1] This approach of his is entirely distinct from his treatment of the power spectrum described previously.

An analytical transformation then gives the corresponding Power spectrum as

$$G(\nu) = \Re e\left[\frac{2\pi A(C - iB)}{(C - iB)^2 + (\nu/2\pi)^2)^{3/2}}\right] \qquad (7)$$

The coefficients A, B, and C required in the above formulas are given in Table 4.9. This approach has many desirable properties. In particular, the PSF derived from it using either approach are positive in practice, and the autocorrelation method in the ultraviolet should work well. At very large angles it presumably breaks down, as all the fits make the PSF fall as θ^{-3} asymptotically. It also fails to give a full description if, as we suspect, the bandpasses of the different measurements do not overlap. Although in practice the total PSF is positive over the range of parameters applicable to ST, something in principle is wrong as the power spectra are not positive definite. About 3% of the power in the residual and subaperture fits comes out negative.

Measurement	A	B	C
PM Full Aperture residuals	$4.45\ 10^{-5}$	.1689	.1209
PM Sub Aperture	$2.48\ 10^{-5}$	1.05	.647
PM FECO	$7.29\ 10^{-6}$	50.0	0.0

Table 4.9. *A summary of the Kenyon and Duerig results on the primary mirror microroughness. The roughness autocorrelation function is then given by Equation 6 in waves^2 if ν is given in cm^{-1}. The corresponding Power spectrum is given by Equation 7 in waves^2 cm^2 when r is in cm.*

All three of the approaches outlined above are implemented in our Telescope Image simulator. It is up to the user to choose the approach that best suits his application, and to carefully consider its applicability Figures 4.3 to 4.5 show the results of applying each of the above three approaches to the same wavelengths respectively.

4.3.3   Effect on ST Observations

Figures 4.6 and 4.7 provide a summary of ground-based observations of the point spread function. Overlayed is a plot of the predicted level of scattered light based on the Brown and Burrows parameterization, and a theoretical seeing profile calculated from atmospheric turbulence theory. Two conclusions are evident. First, the ground based data is limited by the seeing, and indeed follows the seeing prediction remarkably accurately. Second, the scattered light level predicted for ST is much higher than the seeing background in the wings of the PSF. It follows from this that **measurements of extended sources that are limited by nearby bright sources that are more than about two arcseconds away at visible wavelengths are best done from the ground.**

A more detailed description of the data analysis that lead up to these Figures is included below. Images of the occulted supernova 1987A in the B and R bandpasses were analysed. The data was subjected to standard reduction algorithms, which subtract bias based on overclocked pixels, subtract dark exposures, and flat-field. Cosmic rays were removed by identifying those pixels that differ from their neighbours by 3 sigma more than the average
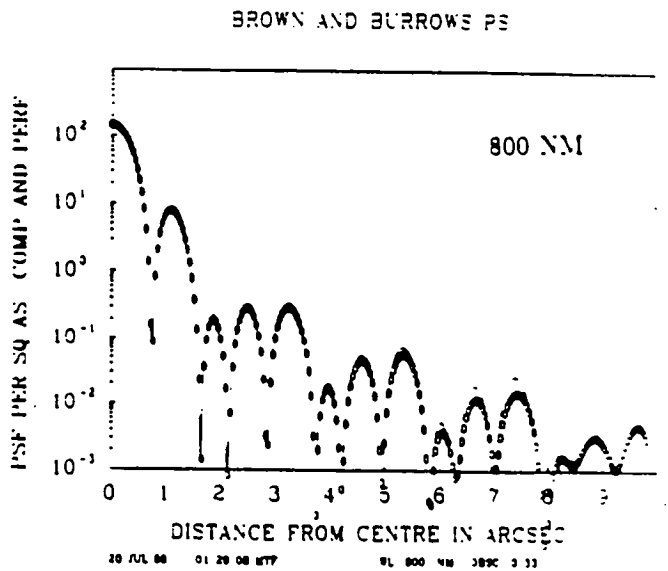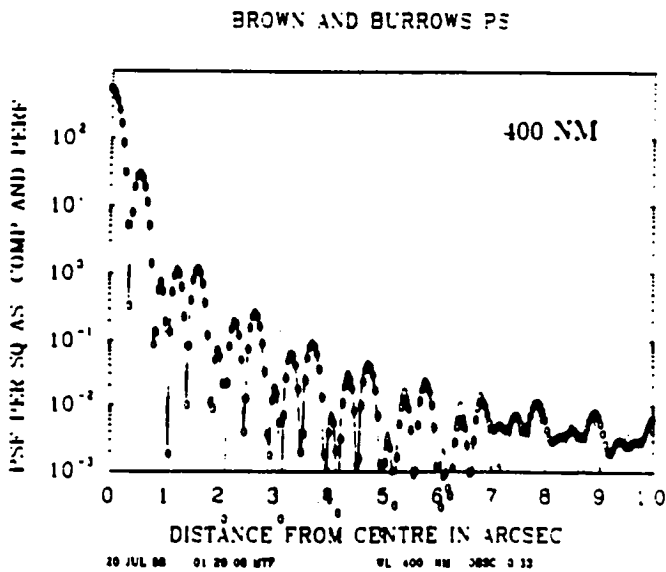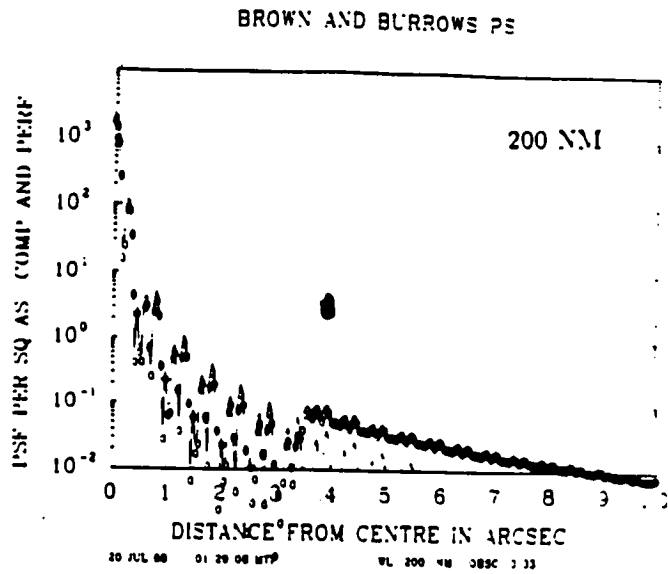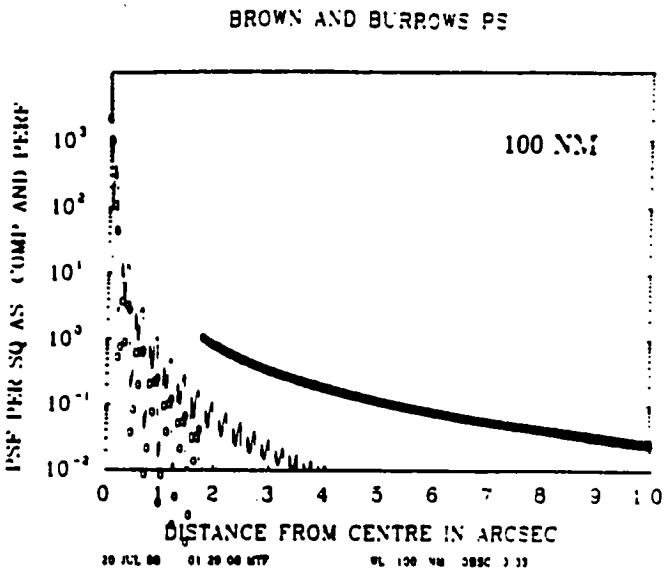
Figure 4.5 A montage of the predictions obtained using the power spectrum fit of Brown and Burrows, normalised to unit total integral. Plotted is the power per square arcsecond, against the distance from the source center in arcseconds. For simplicity, no other errors such as jitter or surface dust scattering are included. In each panel, the PSF both with and without microroughness is plotted.
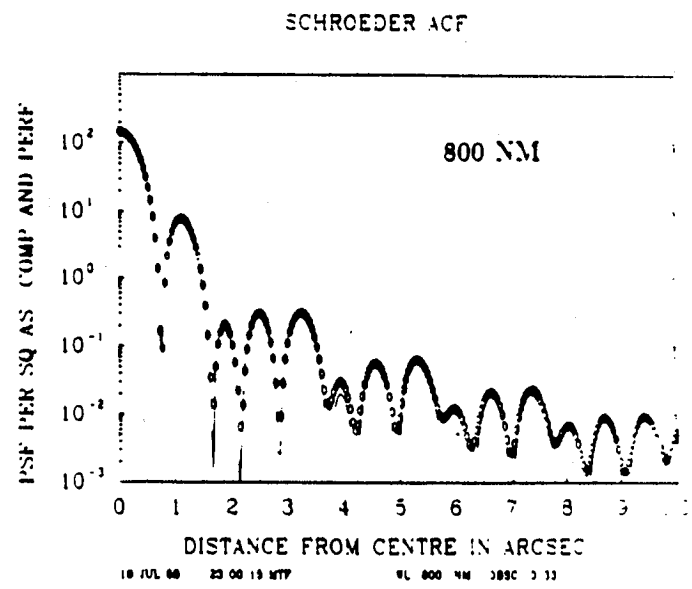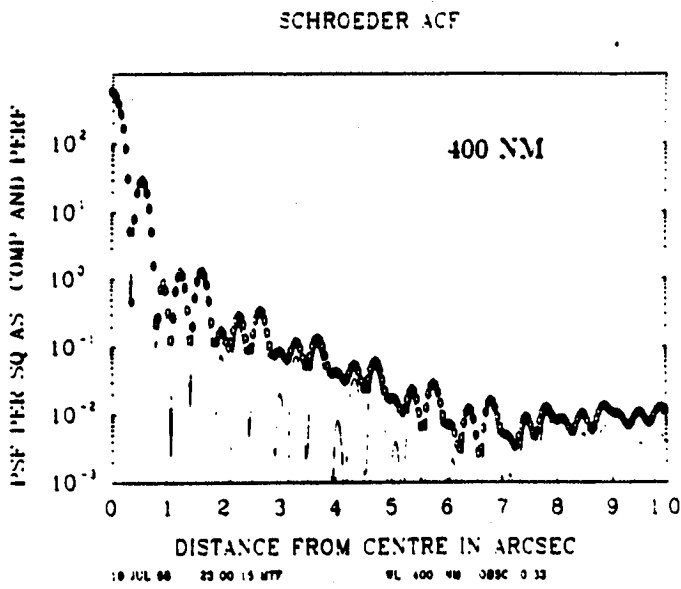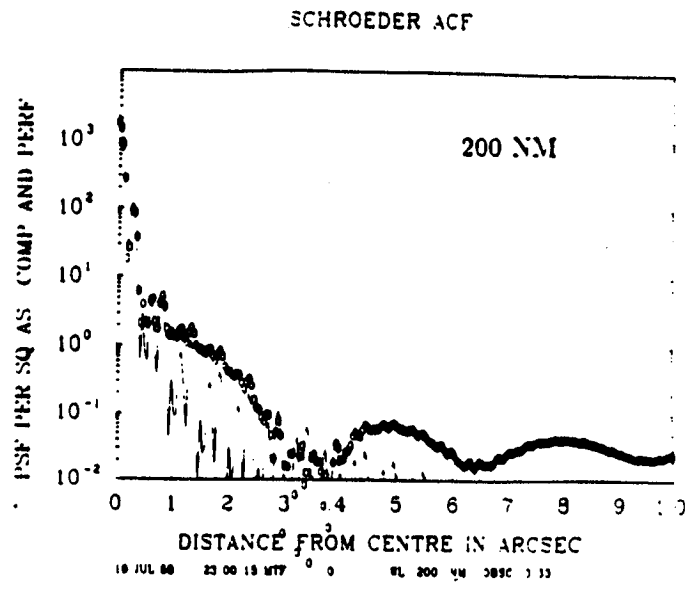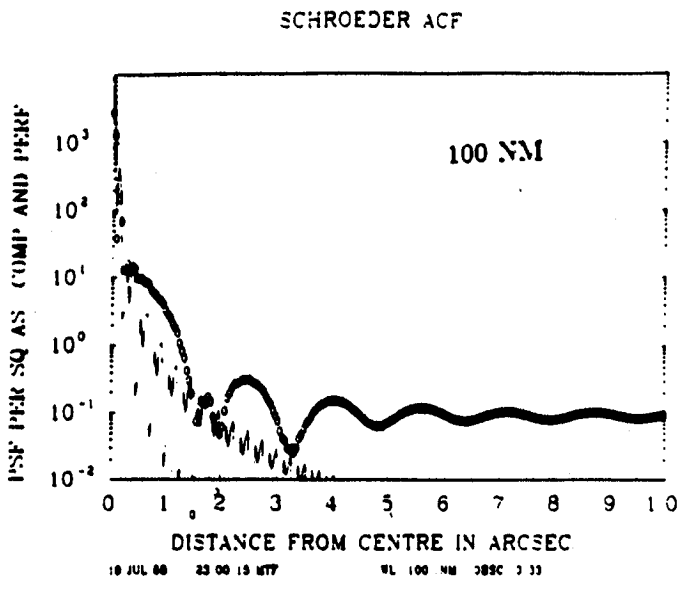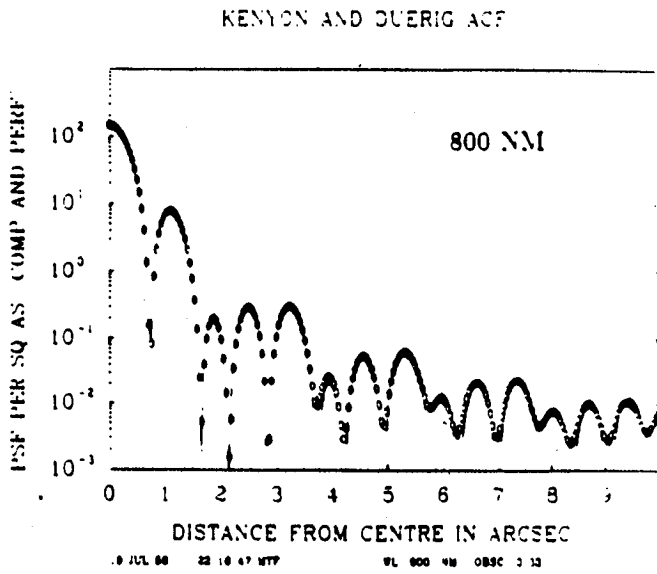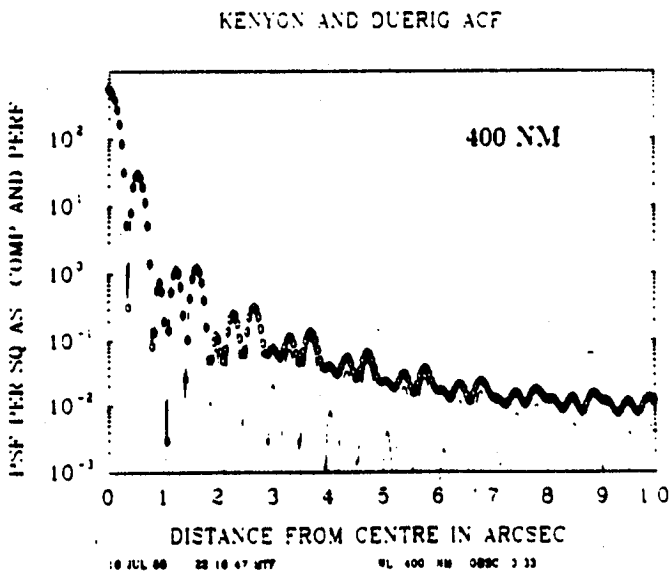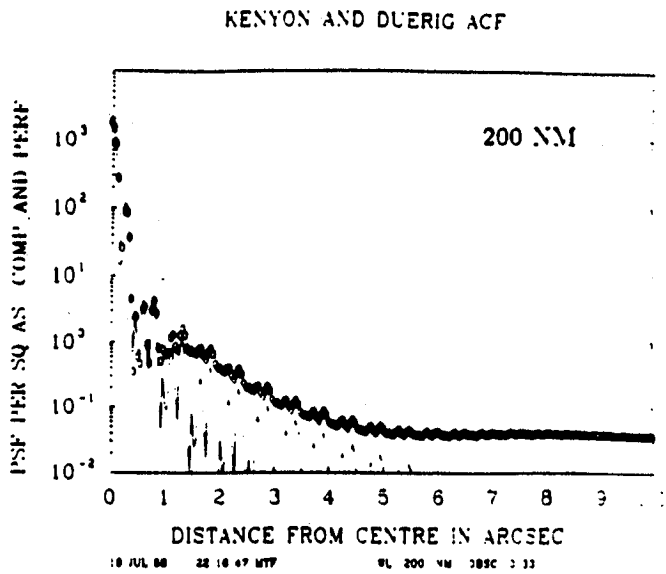
Figure 4.6 A montage of the predictions obtained using the autocorrelation function fit of Schroeder, normalised to unit total integral. Plotted is the power per square arcsecond, against the distance from the source center in arcseconds. For simplicity, no other errors such as jitter or surface dust scattering are included. In each panel, the PSF both with and without microroughness is plotted.
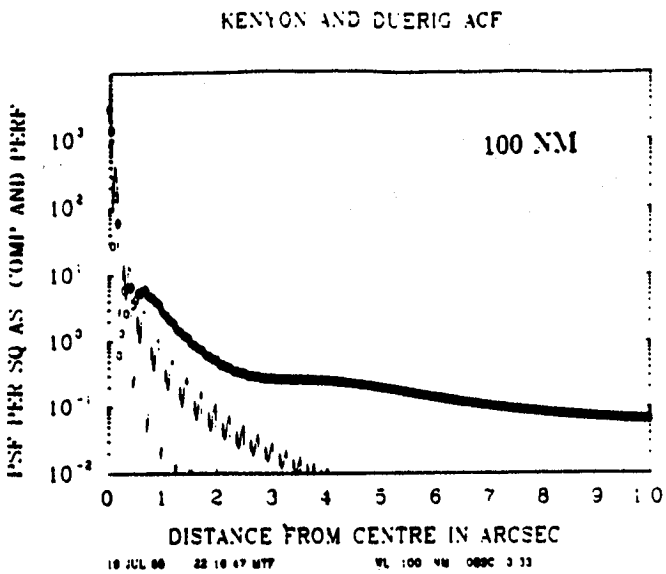
Figure 4.7 A montage of the predictions obtained using the autocorrelation function fits of Kenyon and Duerig, normalised to unit total integral. Plotted is the power per square arcsecond, against the distance from the source center in arcseconds. For simplicity, no other errors such as jitter or surface dust scattering are included. In each panel, the PSF both with and without microroughness is plotted.

statistical noise, as a function of intensity. They are replaced by bilinear interpolation where possible, or masked out entirely. This interpolation is permissible as our plate scale is such that about 10 pixels cover the seeing disk diameter. All bad pixels are masked out, and do not contribute to the subsequent analysis. This includes bad flat field pixels defined as having an apparent QE more than a factor of 2 different from the average, bad columns, uncorrected cosmic ray events, pixels within the geometric image of the occulting wedge, and overclocked pixels.

The theoretical seeing profile is well understood through atmospheric turbulence theory, and the associated effects of the turbulence on the structure function of the wavefront. The expectation of the point spread function (which is equal to its time average in a long exposure) can be derived by multiplying the telescope diffraction OTF by an atmospheric MTF, and performing a Fourier transform.

The telescope OTF was approximated with the appropriate function for a circularly symmetric aperture with a central obscuration, and zero wavefront errors. The atmospheric MTF depends on only the Fried parameter r_0, which is roughly the size of a telescope aperture that would give a diffraction limited image of the same size as the seeing disk. Thus, the theoretical profile depends on only one parameter. That parameter in turn, is completely fixed by the FWHM of the seeing profile, which is determined from a background star in the image. Therefore using the theoretical profile normalised from the photometry of the supernova, gives a **parameter free** prediction of the observed wings of the seeing profile.

The seeing profile varies slowly with wavelength. I used wavelengths of 400nm for the B bandpass and 600nm for the R bandpass, when computing the theoretical profiles. Although these wavelengths are not exactly the effective wavelengths of the bandpass, the error introduced is small. The Fried parameter r_0 (at a fiducial wavelength of 500nm) came out as 16.5cm for both bandpasses. This shows that the atmospheric conditions were virtually identical for the two exposures. The corresponding FWHM of the Gaussian fits are 0.813 for the B band image and 0.879 for the R band image.

The azimuthally averaged radial profile is plotted in Figures 4.6 and 4.7. Only pixels that were not masked out for any reason are included in the averaging process. It is easily seen that the agreement between the theoretical and observed curves is excellent, even though no parameters are available to vary. The theoretical profile was not continued beyond 10 arcsec because of numerical instabilities in the Hankel transform routines used to compute it. Coincidentally, at distances of about 10 arcseconds, the average radial profile flattens, while the seeing profile will continue to drop. The flattening is due to scattering from the mirror surfaces, or to background light. This data was obtained at the ESO 2.2 m telescope with Francesco Paresce. See Ap J. (letters) 337, L13 (1989) for a discussion of the scientific implications for the SN.
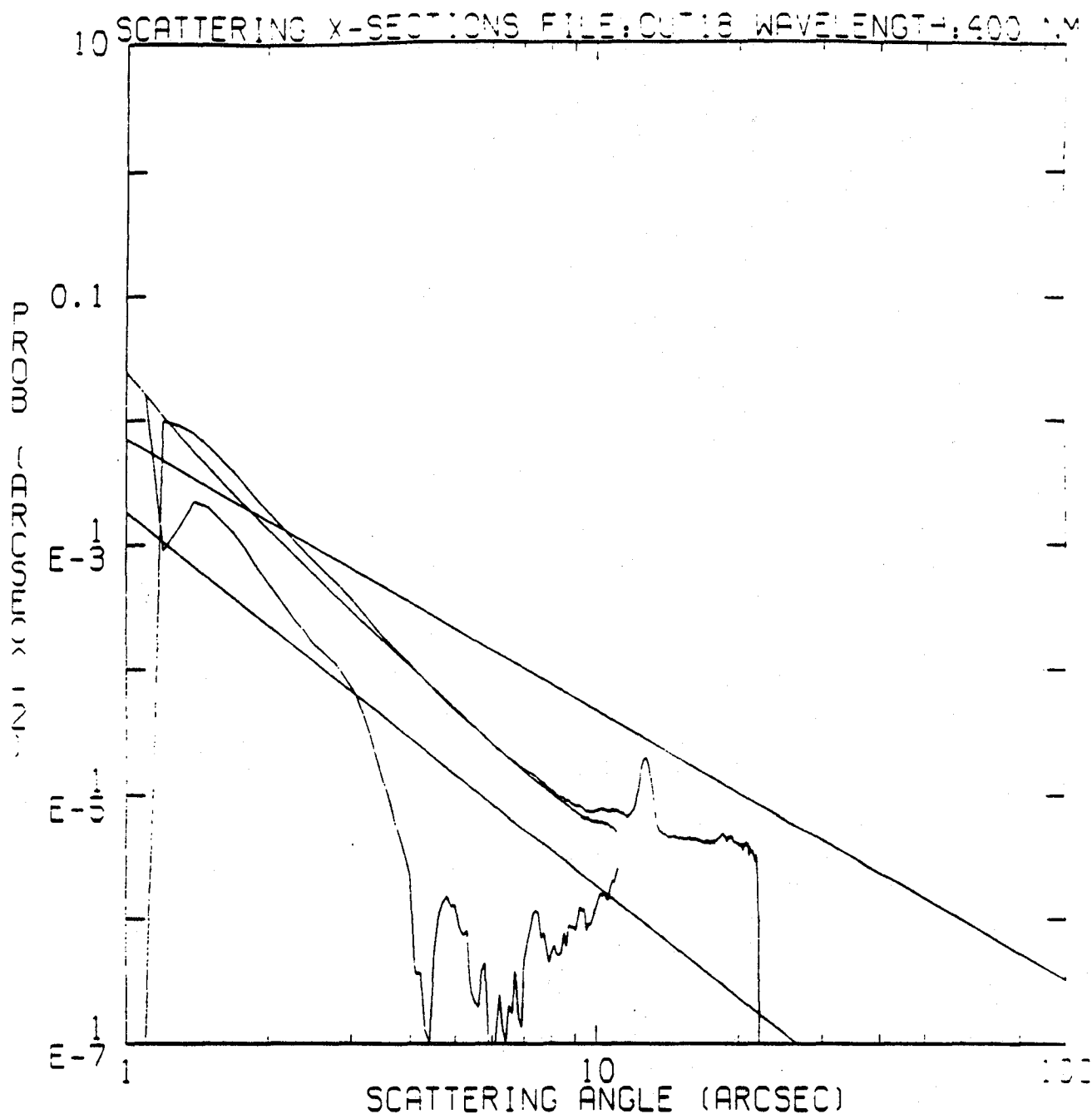
Figure 4.8 A plot of ground-based coronographic measurements of the wings of the seeing profile, compared to the predictions of atmospheric turbulence theory, and to the wings predicted if the primary mirror has the same microroughness power spectrum as that of ST as estimated by Brown and Burrows. Also shown is the curve obtained in the diffraction limit. Observed data plotted here is for a B band exposure, while the theoretical curves are computed at a wavelength of 400 nm.
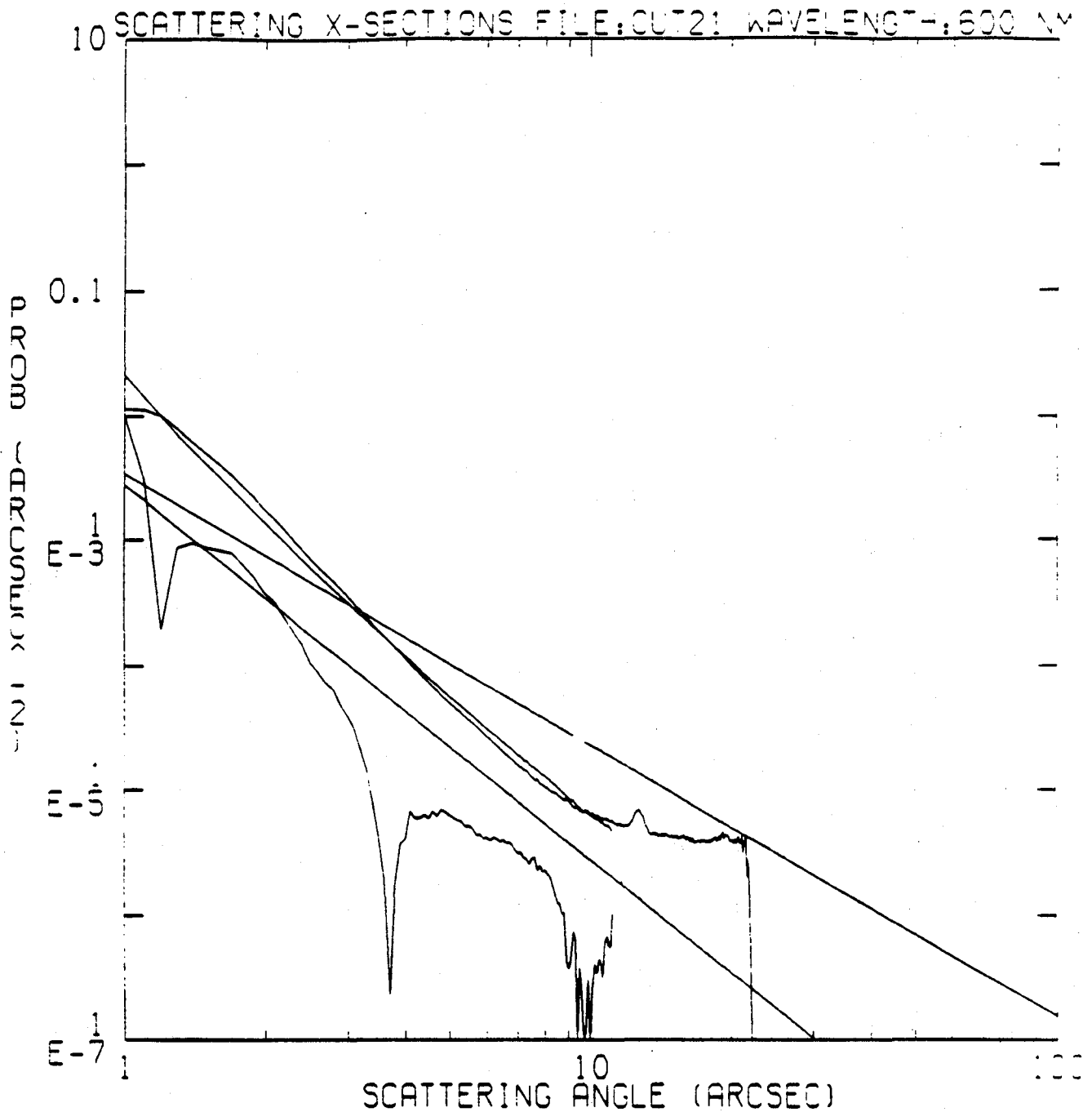
Figure 4.9 A plot of ground-based coronographic measurements of the wings of the seeing profile, compared to the predictions of atmospheric turbulence theory, and to the wings predicted if the primary mirror has the same microroughness power spectrum as that of ST as estimated by Brown and Burrows. Also shown is the curve obtained in the diffraction limit. Observed data plotted here is for a R band exposure, while the theoretical curves are computed at a wavelength of 600 nm.

5.0   SIMULATION SOFTWARE

Software is available to simulate the ST imaging of orbiting sources. The software includes all known effects on the PSF, and detector defects for the WF/PC. This chapter outlines the capabilities of the software. A more detailed users' manual, and copy of the software and database is available on request.

5.1   DETECTOR CHARACTERISTICS

The detectors considered in the simulation are two dimensional with rectangular pixels. This includes all the SIs for ST at least in suitable limits. The simulation allows a general astronomical scene to be imaged onto such a detector, with the integration over pixels, wavelength dependances, and throughput modelled comprehensively. The detector can suffer from various defects such as saturation, charge transfer problems, wavelength dependent flat field variations and so on. Various other effects such as background, photon noise and readout noise can be readily introduced.

The uses of an adequate image model are manifold, therefore it is imperative that the results provided as standard be as complete as possible. The results provided as standard options are listed in the following section.

5.2   OUTPUTS AVAILABLE

5.2.1   Image Descriptions

The fundamental output from the entire software package is a simulated image of an astronomical scene for a given SI. The images are available as STSDAS/IRAF compatible data sets (.HHH and .HHD files). All other intermediate images are also available in this format. Other outputs are available that characterise the image as described below.

The image quality in a given plane at a given wavelength at a given position in the field of view can be described completely for incoherent illumination by the point spread function (PSF). This is the intensity at a given two dimensional displacement from the Gaussian image of a point monochromatic source. It is normalized so that the integrated intensity is unity. The PSF is therefore a function of six variables for an object at infinity: 3 coordinates in image space, 2 in object space, and wavelength. It is customary to sample this function as follows:

1. Provide data at a small number of points in the field of view. These would normally include the center of the FOV, the edge, and perhaps an intermediate point, in two orthogonal directions. The user has control over the number and placings of the points used.

2. Provide data at a small number of wavelengths. For visual optical systems, three wavelengths are normally used. The large spectral range of ST necessitates more for some applications. The system is designed to handle up to twenty six. It will enable weighted averaging over wavelengths to simulate realistic bandpasses.

3. Provide sampled data at one focal plane. This will normally correspond to the detector plane. The sampling includes integration over pixel area if required.

At each field point and wavelength combination, one two dimensional function needs to be specified. There are many ways of displaying aspects of this function. All of the following are supported.

1. Provide a two dimensional contour or perspective plot of the PSF.
2. Provide graphs in given directions. Often chosen are the intersections of the tangential and saggital planes with the image plane.
3. Provide similar contour, perspective and directional plots of the MTF (the modulation transfer function). This is the amplitude of the Fourier transform of the PSF.
4. Provide Encircled Energy (EE) curves against distance from the image center.
5. Provide wavefront error maps on the entrance pupil.
   The above outputs are sufficient to characterise the image. To better understand the image, one can produce the following information as required:
1. The diffraction limited PSF. This includes the secondary obscuration but not the pad or spider contributions.
2. The asymptotic PSF. A formula has been derived for the diffraction PSF in the wings with nonzero low frequency aberrations. See Section 4.2.7. These functions can be overplotted or subtracted from or divided into the PSF in any direction or order. Plots on linear or logarithmic scales are available.

5.2.2 Performance Measures

The output detailed in section 2.2.1 is useful in understanding the image quality and for some analytical work. However several numbers that can be derived from the PSF are in common use as measures of image quality. They provide convenient means of quantitatively comparing performance at different wavelengths, positions and configurations. The following are provided:

1. The Strehl ratio of the PSF at the image point with maximum intensity to its value in the absence of aberrations. When this value is greater than 0.8, one speaks of close to diffraction limited performance.
2. The Rayleigh resolution limit. This is the separation of two point sources at which the first minimum of one coincides with the maximum of the other. It is only a rough guide to the resolution.
3. The Sparrow resolution limit. This is the maximum separation of two sources at which the combined intensity profile given as the sum of the PSFs has no saddle point between the Gaussian image points. It is equal to 0.82 of the Rayleigh limit for the diffraction pattern of a circular aperture (Airy disk). It is a better guide than the Rayleigh criterion, particularly if aberrations or jitter have significantly moved or even eliminated the first minimum. The definition also works for sources of differing intensities.
4. The magnitudes of individual aberrations are useful for understanding the behaviour of the PSF as a function of position and wavelength. One must have the third order spherical aberration, astigmatism and coma coefficients which influence image quality. However for ST these are typically so well corrected that the higher order coefficients are important. This software is an improvement over all commercially available alternatives in that it gives the aberration coefficients to high order for general decentered systems.

5.3 PROGRAM STAGES

The computation of quantities of physical interest such as a mean photon count in a given detector element proceeds in a sequence of well-defined and modular steps. At each step some output becomes available that reveals more about the optical system. For each step we indicate below, the input, processing and output. Each step is implemented as a separate executable image, controlled by its own command procedure.

The basic steps in program execution are:

1. Generation of Zernike polynomial coefficients for clear apertures using a commercial software package, CODEV.

2. Computing a wavefront map from the above coefficients and fitting to generate Zernike polynomial coefficients for 0.33 obscuration. A set of files containing the Zernike polynomial coefficients at some standard wavelengths are provided.

3. Computation of the amplitude spread function. At this stage a description of the aperture in addition to the Zernike polynomials is required.

4. Computation of the point spread function (PSF) and/or modulation transfer function (MTF). Options include the effects of mirror irregularities, dust and jitter. Output consists of the PSF sampled at a particular interval (critical sampling).

5. Resampling the PSF onto a finer/coarser grid, or computing the PSF integrated over the detector pixels. Frequently, the PSF is integrated over the detector pixels, but at a smaller spacing so that the effects of point source registration with respect to pixel boundaries can be included in the next step.

6. Construction of a detector model. This is done in two steps. In the first step, a polychromatic simulated image is obtained for an ideal detector with the option of including flat fields. Options exist to obtaining a sampled polychromatic PSF of a single point source or an image of a star field.

7. Modelling the detector response. At this stage the user has an option to add a background to the image as well as include a variety of detector effects.
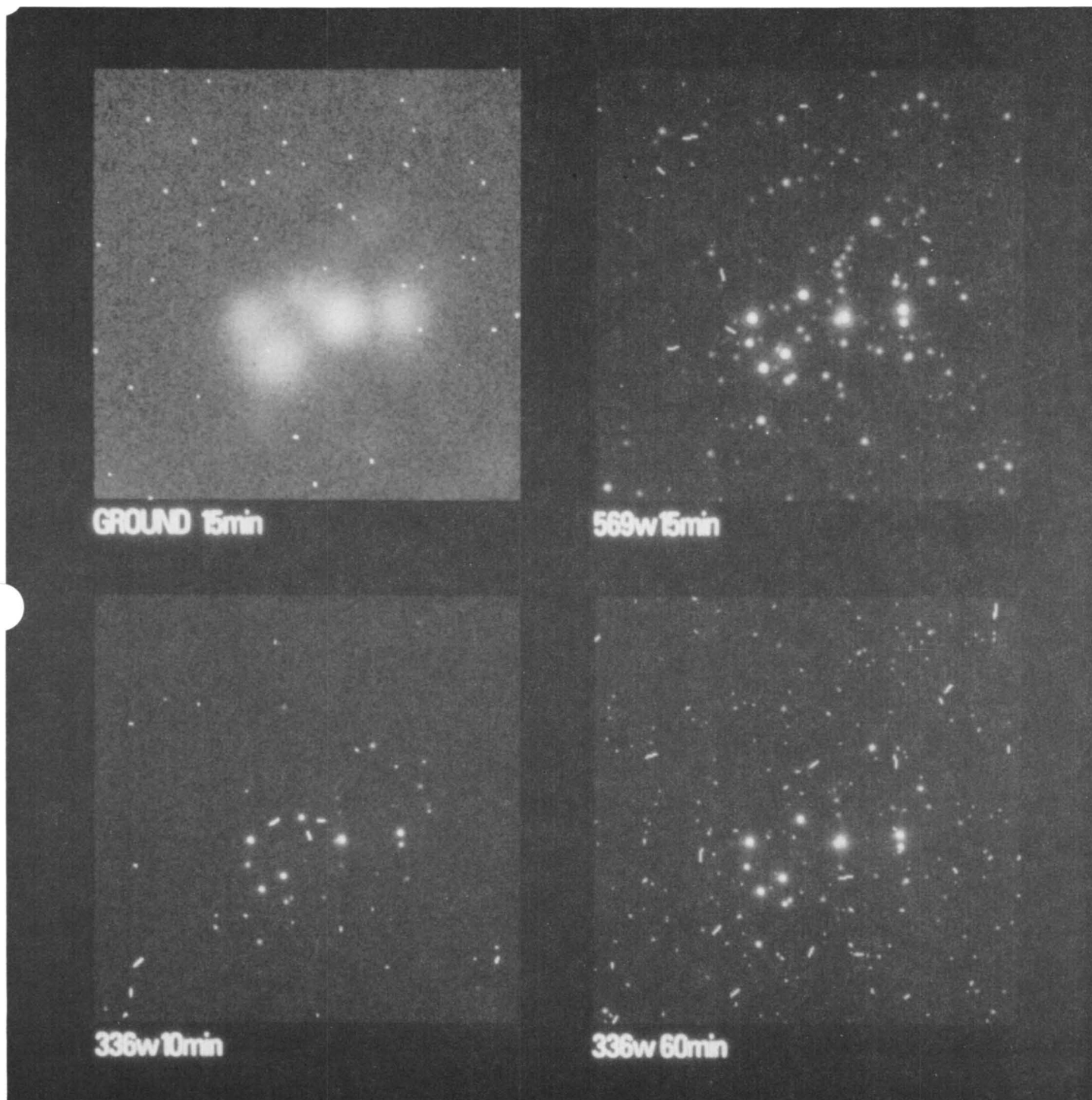
Figure 5.1 Example of simulation software output. The (imaginary) target field is the Pleiades and by a factor 1000 further away (beyond the Magellanic Clouds). The panels show 256 × 256 subimages obtained with the PC from the ground (with 1 arcsec seeing) and through F569W for 15 minutes or F336W for 10 and 60 minutes.